UNIVERSIDADE
BEIRA INTERIOR

Design and Experimental Study of a 3D-Printed Wing with a Morphing Trailing Edge

(versão corrigida após defesa)

João Correia de Pinho

Dissertação para obtenção do Grau de Mestre em
Engenharia Aeronáutica
(Ciclo de estudos integrado)

Orientador: Prof. Doutor André Resende Rodrigues da Silva

março de 2023

Declaração de Integridade

Eu, João Correia de Pinho, que abaixo assino, estudante com o número de inscrição 39680 de Engenharia Aeronáutica da Faculdade de Engenharia, declaro ter desenvolvido o presente trabalho e elaborado o presente texto em total consonância com o **Código de Integridades da Universidade da Beira Interior**.

Mais concretamente afirmo não ter incorrido em qualquer das variedades de Fraude Académica, e que aqui declaro conhecer, que em particular atendi à exigida referenciação de frases, extratos, imagens e outras formas de trabalho intelectual, e assumindo assim na íntegra as responsabilidades da autoria.

Universidade da Beira Interior, Covilhã 27/03/2023

Assinado por: **João Correia de Pinho**
Num. de Identificação: 15161070
Data: 2023.03.27 14:35:41+01'00'

CHAVE MÓVEL

Agradecimentos

Sempre me disseram que se fosse fácil, não era para mim! De facto, esta caminhada não foi fácil, mas só foi possível terminá-la graças a um conjunto extraordinário de pessoas a quem venho deixar o meu mais sentido agradecimento:

Em primeiro lugar, tenho de deixar o meu reconhecimento ao Professor Doutor André Resende Rodrigues da Silva, orientador desta dissertação, por ter aprovado a minha proposta e me ter dado a chance de poder redigir a mesma numa área que despertou o meu interesse desde há muito tempo. Obrigado por ter arriscado juntamente comigo no estudo deste tema!

Não posso deixar de salientar o apoio, os meios e a disponibilidade dos professores Manuel Carlos Gameiro da Silva e Almerindo Domingues Ferreira do Departamento de Engenharia Mecânica da Universidade de Coimbra, e por me terem cedido as suas instalações quando eu mais precisei para poder prosseguir com o meu trabalho!

Queria também deixar uma palavra de reconhecimento à Fundação para a Ciência e Tecnologia (FCT) por me ter apoiado financeiramente com o projeto número UIDB/50022/2020 e pela bolsa atribuída pela Fundação para a Ciência e a Tecnologia com referência BI 03. Verão com Ciência_AEROG.

Em quarto, mas não menos importante, quero agradecer ao AEROG (Aeronautics and Astronautics Research Center) e a todos os membros integrantes. Nada disto seria possível se não fosse pela vossa ajuda, conselhos e palavras de apoio, mas também pelos momentos de descontração e convívio vividos nestes últimos tempos. No entanto, tenho de dar um especial agradecimento ao Emanuel Camacho e à Joana Santos Silva, que foram quem mais vivenciou os desafios e as conquistas desta dissertação comigo, e sei que já vos disse isto muitas vezes, mas obrigado por terem estado sempre a meu lado, na tristeza e na euforia!

Seguidamente, não posso deixar passar sem agradecer àqueles que percorreram todo este percurso académico comigo, e a quem eu tenho o prazer de poder chamar de amigos! Nunca esquecerei o quanto todos me ajudaram a crescer e possibilitaram tornar-me numa pessoa melhor. Um abraço para todos, em especial para o Samuel, Miguel, Ricardo e Nuno, que estão comigo desde o primeiro dia. E que estas amizades sejam para sempre!

Por último, o agradecimento mais importante, fica para a minha família. Ao meu pai, António, e à minha mãe, Isabel, deixo um obrigado do fundo do coração por nestes cinco anos e meio me terem dado apoio condicional em todos os aspetos, e por serem a minha luz quando me encontrava no meio da escuridão. Aos meus irmãos, Ana, António e Pedro, obrigado por sempre contribuírem com sorrisos, brincadeiras e conselhos quando eu mais precisava! E também não posso esquecer os meus avós, tios e primos. Espero ter deixado todos vocês orgulhosos do caminho que percorri, e que nunca me abandonem no que ainda está para vir!

Resumo

Nos últimos anos, há um crescente interesse em tecnologias de *morphing*. Muitos *designs* têm vindo a ser desenvolvidos, com diferentes níveis de complexidade no que diz respeito à fabricação. O principal objetivo desta dissertação é apresentar o desenvolvimento de uma asa com bordo de fuga deformável, de fácil fabrico e controlo, e que permita a execução de estudos aerodinâmicos em túnel de vento de forma viável. Utilizando ferramentas de desenho computacional e impressão 3D, uma asa controlada de forma simples através de componentes básicos é desenvolvida, fabricada e estudada recorrendo a visualização do escoamento e medição de forças. Todo os passos de desenvolvimento são descritos em detalhe, bem como toda a calibração dos equipamentos necessários para reprodução do resultado final, de forma a permitir que outros procedam com uma investigação mais aprofundada da matéria recorrendo ao *design* apresentado. Considerando alguns estudos iniciais, a visualização do escoamento mostrou que a presença da curvatura retarda a ocorrência de perda quando comparada à configuração simétrica, onde a separação começa logo no bordo de ataque. Além disso, o aumento da deflexão traduz-se num aumento do tamanho da esteira produzida, apesar de esta não ter uma reflexão significativa na posição onde o escoamento separa. Relativamente à medição de forças, verifica-se que a curvatura desempenha um papel importante no aumento da sustentação, bem como atrasa substancialmente a entrada em perda da asa, quando se combina ângulo de ataque inicial com deflexão do bordo de fuga. Este *design* permitirá realizar uma ampla gama de estudos, tais como comparar com configurações convencionais de *flaps* para verificar o desempenho de ambos os sistemas, mas também o estudo de condições dinâmicas, incluindo movimentos repetitivos de deflexão do bordo de fuga, que poderão oferecer uma nova configuração no *design* de superfícies aerodinâmicas.

Palavras-chave

Morphing, Asa impressa em 3D, Deflexão do bordo de fuga, *Design*, Visualização, Medição de forças, Perda aerodinâmica.

Abstract

In recent years, the interest in morphing technologies has been continuously growing. Many designs have been developed, but some are very complex to manufacture. The main goal of this dissertation is to present the development of a wing design with a morphing trailing edge that is easy to manufacture and control while allowing the execution of appropriate aerodynamic studies in a wind tunnel. Using computer-aided design and 3D (Three-dimensional) printing, a wing that is simply controlled with easy-to-use hardware is developed, manufactured, and studied using flow visualization and force acquisition. The whole developing steps are described in detail, as well as all the calibration processes of the required equipment to reproduce the final result, in order to enable others to proceed with further investigation using the present design. Considering initial studies, flow visualization showed that the presence of curvature delays stall when compared to the non-deflected configuration, where flow separation starts right at the leading edge. Also, the increase in deflection translates into an increase in the size of the wake, but not having a significant impact on the location of flow separation. In terms of force measurements, curvature plays an important role regarding lift enhancement, as well as substantially delaying wing stall when combining angle of attack with no flap deflection with trailing edge deflection. This design will allow for a wide range of studies to be performed, such as comparisons with conventional flap configurations to verify the performance of both systems, but also the study of unsteady conditions, including the dynamic motion of the trailing edge deflection, which can offer insights concerning aerodynamic surfaces design.

Keywords

Morphing, 3D-printed wing, Trailing edge deflection, Design, Visualization, Force measurement, Stall.

Contents

List of Figures

Nomenclature

b	Wing span	[m]
c	Aerodynamic chord	[m]
C_D	Drag coefficient	[-]
C_L	Lift coefficient	[-]
C_M	Moment coefficient	[-]
d	Distance between balance axis and strain gauges	[m]
D	Drag force	[N]
f	Motor frequency	[Hz]
L	Lift force	[N]
M	Pitching moment	[N m]
m	Calibration parameter	[-]
P	Pressure	[hPa]
q	Dynamic pressure	[hPa]
Re	Reynolds number, $\rho U c/\mu$	[-]
S	Wing area	[m^2]
T	Temperature	[K]
U	Equivalent airspeed	[m/s]
V	True airspeed	[m/s]
α	Angle of attack	[°]
α_0	Angle of attack with no flap deflection	[°]
δ	Servo shaft angle	[°]
θ	Trailing edge deflection	[°]
μ	Fluid dynamic viscosity	[Pa s]
ρ	Fluid density	[kg m^{-3}]

List of Acronyms

2D	Two-dimensional
3D	Three-dimensional
ABS	Acrylonitrile Butadiene Styrene
ARCS	Airfoil Recambering Compliant System
AEROG	Aeronautics and Astronautics Research Center
CFD	Computational Fluid Dynamics
DEM	Departamento de Engenharia Mecânica
FDM	Fused Deposition Modeling
GND	Electrical Ground
LE	Leading edge
LED	Light Emitting Diode
NACA	National Advisory Committee for Aeronautics
PLA	Polylactic acid
TE	Trailing edge
UC	Universidade de Coimbra
VCC	Voltage Common Collector

Chapter 1

Introduction

1.1 Motivation

The human being had the desire of flying since the beginning of time. Observing the natural world that surrounded it, many pioneers invented flying mechanisms throughout history, such as the kite [1] in 1200 a.C. Further in history, through the observation of birds' motion and wings, Leonardo da Vinci paved the way for the first construction of a flying machine [2]. Later in 1903, the Wright Brothers, taking inspiration from eagle wings, performed the first successful human flight in a powered airplane [3]. Although being from different eras, the work from both pioneers are excellent examples of the influence of biomimicry applied to aeronautics, stimulating the development of the modern aircraft.

The term "Biomimetics" derives from the Greek, being the junction of the words life (*Bios*) and imitation (*mimesis*) [3], meaning that it is an area of investigation whose main objective is the study and development of innovative technologies that imitate nature and biological systems. Those can be applied in various fields of investigation, such as physics, biology, chemistry, engineering, computer, and material sciences, as seen in Figure 1.1. Through the years, the interest in the study of biomimetics has been growing exponentially [4], matching the increase in the number of publications on this subject, as seen in Figure 1.2. This increasing interest resulted in the evolution of the concept from simple imitation of natural organisms to integration and combination with modern science and engineering in order to create new structures, materials, and applications [3].

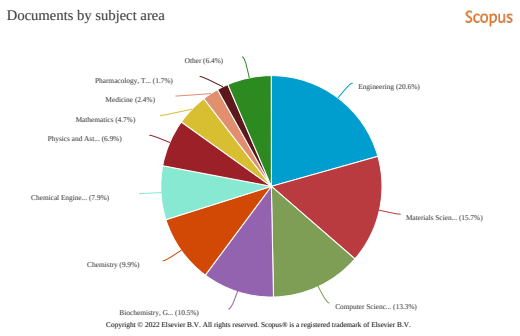

Figure 1.1: Published documents by subject area with the keyword "Biomimetics".

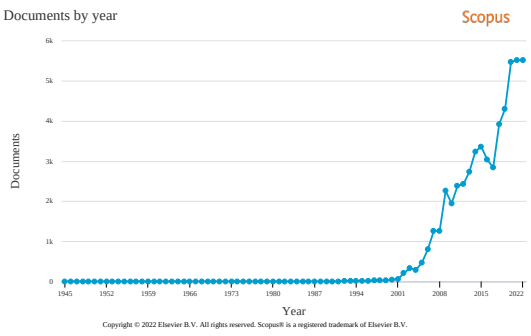

Figure 1.2: Published documents by year with the keyword "Biomimetics".

From a biomimetic perspective, avian morphology had a big influence on past and current research in the aeronautical fields related to aerodynamic efficiency. The wings of a bird are composed by several consecutive rows of flexible covering feathers that act as an array

of movable flaps to manage the resultant aerodynamic force during flying. Birds can also reduce wing drag while flying through the deployment of a few feathers [5]. The observation of this continuous change in shape and size of the wings has been more and more studied by designers through the years with the main goal of increasing aerodynamic performance [1, 6]. Despite aircraft not flapping their wings, birds serve as inspiration for aircraft and wing design.

The idea of changing the wing shape is not a recent innovation. The Wright's Flyer had flexible wings that would adapt depending on the flight phase to successfully control the aircraft while performing different maneuvers [7]. However, since the current market is quite conservative, new technologies take many years before being commercially applied. Aircrafts are designed with a specific mission profile and have to compromise their performance in off-design flight conditions [1], and require movable devices to improve flight control, such as flaps and ailerons.

Morphing aircraft can be defined as an aircraft that significantly changes its configuration in order to maximize its performance in distinct flight conditions and in flight. These adjustments can be performed in various parts of the vehicle, such as the fuselage, wings, engines, or tail [8]. Conventionally, "morphing" is a term that refers to technologies to improve performance via alternating wing geometry, obtaining an optimized wing shape [9]. These changes can be in sweep, aspect ratio, twist, thickness, and camber. This dissertation mainly focuses on the latter.

It is commonly agreed by most authors that the idea of changing the wing shape or geometry is far from new, but there is not an exact definition or agreement on the type or extent of the changes necessary to qualify an aircraft or aerodynamic surface as "morphed". Morph is short for metamorphose, which can be defined as changes in physical form, structure, or substance, but also as a striking alteration in appearance. Considering the first definition, validated technologies such as flaps and slats can be considered as morphing mechanisms. However, the concept of striking alteration imposes the connotation of radical shape-changes in the aerodynamic surface, and this is what causes disagreement between authors when it comes to conventional control surfaces [10].

For the remainder of this dissertation, shape change through control surfaces such as flaps and slats will be considered as conventional high-lift mechanisms while, otherwise, morphing technologies adapt to the flow conditions through structural deformation instead of rigid body movements, leading to conformal systems and smooth structural surfaces [11].

1.2 Literature Review

Throughout the years, many techniques have been developed and studied to improve performance in aerodynamic surfaces. One of those surfaces are flaps, which have been the most commonly used technology to increase lift in airplane wings in different flight conditions [12].

During take-off, the extended flaps are used to reach the necessary lift at the lowest speed possible. Similarly, on landing, they are used to minimize the aircraft's speed without stalling. While the aircraft is on cruise, these are not required.

To do so, flaps should be retracted so that only the necessary amount of lift is generated. These changes in lift are reflected in changes in drag. Therefore, it is necessary to find the solution that best balances both forces for each phase of flight [13].

One common problem in conventional flaps is the discontinuous curvature that these aerodynamic surfaces have in the hinge point of the camber line [14]. The discontinuity results in an adverse gradient in the upper and lower surfaces of the wing. On the upper surface, this gradient may result in boundary layer separation, which can be followed by reattachment. Meanwhile, on the lower surface, a recirculation bubble is generated in the hinge zone [15]. These effects have a significant impact on the wings' aerodynamic drag, so solutions have been studied to minimize it.

The most basic structures are the plain flap and the split flap. In the plain flap, the rear portion of the wing airfoil rotates downwards on a simple hinge arrangement mounted at the front of the flap. Flow separation easily occurs when in slightly larger deflections, resulting in losses in lift and increases in drag [16]. Since this is the simplest mechanism, it is also the lightest and has the easiest maintainability when compared to others due to less movable parts and less complexity [17]. However, the amount of lift they can create is somewhat limited. That is why it is currently less used in modern civil aircraft due to more advanced and efficient options being available. As the name suggests, in the split flap, the system is divided into two parts in which only the lower portion can deflect outwards, while the upper surface remains immobile [15]. Similarly to the plain flap, the deflection of the aerodynamic surface results in an increase in lift, but the consequent significant increase in drag and the influence in longitudinal stability make them uncommon these days [18].

A slotted flap is similar to the plain flap, but to further augment lift, it has an air passage between the wing and the flap that reduces the possibility of flow detachment [19]. The gap forces high-pressure air from below the wing over the upper surface of the flap, helping to reduce boundary layer separation and allowing the airflow over the flap to remain less turbulent.

Yet, the most commonly used configuration for mainstream civil aircraft is the Fowler flap

and its derivations due to its good lift increment and reliability. Fowler motion can be defined as the increase in developed wing chord. This is obtained by initially translating a split flap rearward, resulting in an increase in the surface area of the wing [20], succeeded by the rotation of the flap, which results in an increment in camber. Most large aircraft use this system or its variations due to the capability of changing airfoil camber for optimization of performance in both take-off, with partial extension for optimal lift, and landing, with full extension for optimal lift and drag. The double-slotted Fowler flap improves the performance of the Fowler flap by delaying even more the flow separation due to the addition of a level of boundary-layer control not possible with the single-slotted one. It is possible to deflect the flap at even higher angles before flow becomes excessively separated with the addition of extra slots [21].

The different types of flaps previously presented are shown in Figure 1.3.

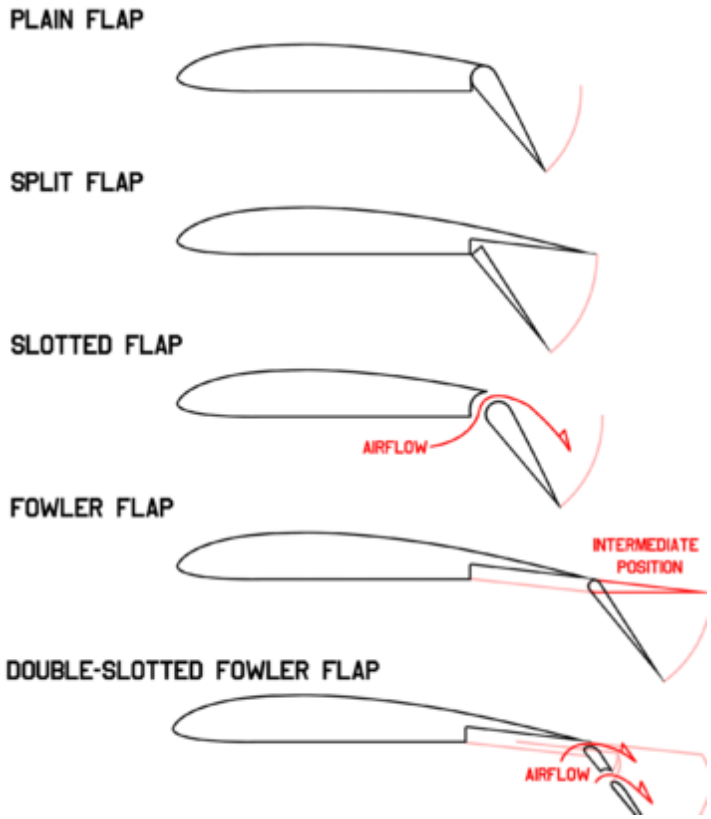

Figure 1.3: Representation of different flap types.

No matter how many solutions for improvement have been developed, there is still necessary to continue developing passive and active flow control technologies that are simple, effective, and low-noise designs so that new-generation aircraft can be even safer, more comfortable, and environmentally friendly. Researchers developed micro vortex generators to control flow detachment by producing controlled vortices that sweep uncontrolled airflow separation over the wings and flaps. The use of these small micro vortex generators has proven to be practical and effective in restraining flow separation on flaps, but the additional drag cannot be neglected [22].

Solutions that provide a smoother camber line curvature combined with a continuous outer surface are in development. However, it is important that these do not compromise the safe and correct handling of the control surfaces. As already stated, to obtain a smoother curvature in the camber line, solutions have been studied, such as Double-Slotted Fowler Flap [23], but also Parabolic Trailing-Edge Flaps with sufficient elasticity so that the trailing edge can be continuous. A continuous trailing edge would eliminate big uncontrolled vortices which otherwise would be formed with the use of conventional flaps due to its discontinuity. The elimination or, at least, reduction of this vortex formation would reduce viscous drag, and acoustic emissions from turbulence could be attenuated [24].

For this reason, the interest in studying morphing technologies for aerodynamic surfaces has been continuously growing. Some authors define morphing wing as an aerodynamic surface that changes its configuration in order to maximize its performance in different flight conditions [25]. Numerical studies show that to produce the same change in lift, a smaller flap deflection is required for parabolic flaps than traditional flaps [26]. A parabolic flap deflects with the camber line conforming to a curved parabolic shape rather than the single-joint articulation of a traditional flap. At the same time, parabolic flaps can reduce up to 50% of the drag when compared to a traditional flap. However, this significant drag reduction happens at high flap-chord fractions. In low flap-chord fractions, the reduction is less noticeable and, in some cases, can even be worse than traditional ones [27].

Combining this airfoil geometry with the use of flexible compliant materials for the skins makes it possible to achieve fully morphed trailing edge sections. Continuous progress has been made on the structural aspects of morphing devices over the last decade, but there is a shortcoming of information regarding the aerodynamic performance of these structures [28].

The biggest challenge in developing morphing wings is to conciliate high load-bearing capacity with the structural flexibility required [29]. A structure consisting of corrugated components can be a feasible solution for this challenge [30]. If the corrugation direction aligns with the wing chord direction, chord-wise morphing would be possible with high stiffness in the span direction [31].

In 2011, Vale et al. [32] performed a numerical study of optimization and performance evaluation of a morphing wing with variable span and camber. They refer to the main problem as the augmentation of drag caused by the discontinuities in the airfoil shape, in the case of flaps. It is stated that increasing the airfoil camber can be beneficial when higher C_L values are required, not only because that higher C_L value before stall is achieved but also because of a higher lift-to-drag ratio. Meanwhile, the presence of a flap generally increases C_L but decreases the lift-to-drag ratio. Camber change without loss of performance would allow for an improved adaptation of the wing for both high and low speeds, using a symmetrical or cambered airfoil configuration, respectively.

The idealized concept consists in actuating a shell with the shape of one airfoil and a specific thickness distribution that deforms into the other airfoil shape. When cambered, the length of the upper surface is larger than the lower one. Therefore, a NACA0012 (National Advisory Committee for Aeronautics) airfoil was slightly modified, resulting in a maximum camber of less than 0.4%, and the aerodynamic differences to the original NACA0012 are expected to be very low. This camber is caused by a discontinuity, visible in Figure 1.4, in the trailing edge, where the boundary layer is thicker, so the geometrical changes should not be important to aerodynamics.

Figure 1.4: Modified NACA0012 airfoil used in [32].

In this CFD (Computational Fluid Dynamics) study, four span configurations were analyzed, with each having four different cambers. These sixteen configurations were analyzed for six different angles of attack at a speed of $30\,\mathrm{m/s}$. Each of these configurations is then compared with an optimum fixed wing with 4.2% camber. It was considered as reference a wing area of $0.8129\,\mathrm{m}^2$. The comparison showed that the most significant penalties of the morphing wing are a reduction in the rate of climb and a slight increase in drag at $30\,\mathrm{m/s}$, which is the speed for which the fixed wing is optimized. The greatest benefits are a reduction in stall speed and a decrease in the glide angle. In general, the morphing wing outperforms the optimum fixed wing, but it is established that further studies are essential to fully assess the morphing benefits.

Later, in 2014, Yokozeki et al. [31] developed and wind tunnel tested a variable camber morphing wing. They developed a wing based on the Wortmann FX63-137 airfoil, with $c = 800\,\mathrm{mm}$ and $b = 800\,\mathrm{mm}$, with the morphing section being defined as the trailing edge after 69% chord position of the airfoil. Relatively to the structure, the core of the morphing section is made of a corrugated structure of which the overall envelope coincides with the shape of the airfoil. In Figure 1.5, a schematic of the corrugated morphing section is shown.

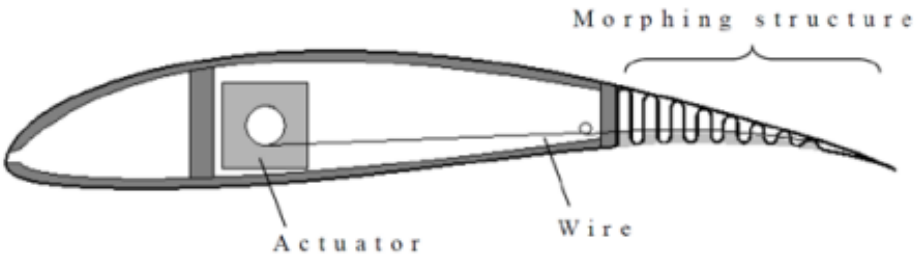

Figure 1.5: Mechanism of the morphing wing used in [31].

It is also visible that a wire is attached to the trailing edge region, passing through the corrugated structure near the lower surface, and then hooked to a servo motor inside the wing.

The rotation of the servo shaft tensions the wire, resulting in downward deflection. This can be achieved by only two actuating systems for the whole $800\,\mathrm{mm}$ span. It should be noted that deformation can be accomplished only downwards using the present mechanism, meaning it cannot be efficiently applied for roll maneuvers. This concept was compared with a reference wing model with a single-hinge aileron at 77% chord position. The manufactured wings were then tested in wind tunnel to determine the aerodynamic forces using a balance underneath the struts. Both wings were tested for deflections between $0°$ and $40°$, for Reynolds up to 1.5×10^6, with the developed design achieving smooth morphing without any system failure.

Results show that the aerodynamic characteristics of the morphing wing are superior to the hinged one. When α is small, the lift coefficients of the morphing wing are high compared to the reference. When θ increases, the polar curve of the morphing airfoil exhibits superior characteristics, in the range prior to stall, when compared to the hinged airfoil. The linear region in $C_L - \theta$ curve is wide in the case of the morphing wing compared to the reference wing, indicating a wide active aileron range and less flow separation in the case of the morphing wing.

Meanwhile, another morphing wing based on compliant structures was being designed, manufactured, and tested by De Gaspari et al. [33], this time with mechanisms to change camber in both leading and trailing edges. A completely new design was developed using PHORMA software to identify the optimal morphing shape to be used as the airfoil. The leading edge has a maximum downward angle equal to $7°$ and the maximum upward and downward droop angle for the TE (Trailing edge) equal to $10°$. The resulting wing has a chord of $418\,\mathrm{mm}$ and span of $930\,\mathrm{mm}$, being limited by wind tunnel dimensions, and was tested for a single velocity of $40\,\mathrm{m/s}$.

The leading edge structural model is characterized by two clamps at the upper and lower connections with the structural interface points, while a horizontal actuation force pushed in the left direction tries to deflect the leading edge downward. A similar procedure was implemented in the trailing edge, but with a much more flexible architecture to allow for upward and downward deflection. The thickness of the surface was defined based on computational stress analyses. As seen in Figure 1.6, both sections are 3D-printed individually and then attached to a wing box that acts as a rigid support for the whole wing, and accommodates the measuring and actuating devices.

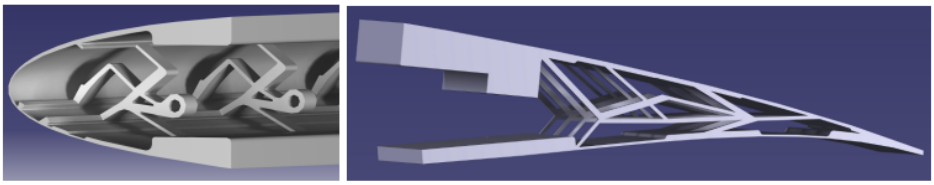

Figure 1.6: Leading and trailing edge models used in [33].

Tests were performed for four configurations: undeformed airfoil, morphing leading edge, morphing trailing edge, and combined morphing leading and trailing edge. Pressure taps

were added in the middle span of the model, where a 2D (Two-dimensional) flow is likely to occur, in order to obtain the pressure coefficient around the airfoil and, consequently, the value of C_L.

The lowering of LE (Leading edge) moves the center of gravity towards the rear, changing the pitching moment, while the deflection of TE increases the maximum value of the suction peak and the area of the curve, thus increasing the generated lift. The combined effect of the two morphing surfaces globally enhances the aerodynamic performance when compared to the reference undeformed shape. For higher incidence angles and speed, the effect of the leading edge is less noticeable. The leading edge causes a small reduction in the amount of generated lift when compared to the undeformed airfoil, but in return it delays stall. On the other hand, the effect of the morphing trailing edge is to substantially increase lift, with a combination of the two resulting in a maximum C_L occurring for a higher value of α, with the leading edge having a bigger influence in stall delay rather than in the previous case. The obtained values were validated with CFD analyses, showing coherent and valid results.

In 2016, Ai et al. [11] conducted an experimental investigation of an airfoil based on the NACA0012 in which they fitted diverse morphing trailing edges having various camber profiles with the same trailing edge tip deflection. The wing, with a chord length of $0.2\,\mathrm{m}$ and a span of $0.45\,\mathrm{m}$ was manufactured in polyurethane, with the final 30% of chord length designed to allow for multiple interchangeable trailing edges with the required camber profile and deflection angle to be attached. Deflections of 5% and 10% were tested, for a range of Reynolds between 3.5×10^5 and 5.6×10^5 and angles of attack from $-5°$ to $20°$. In this experiment, the aerodynamic forces were obtained using a force platform mounted at the base of the setup. The studied configurations are represented in Figure 1.7.

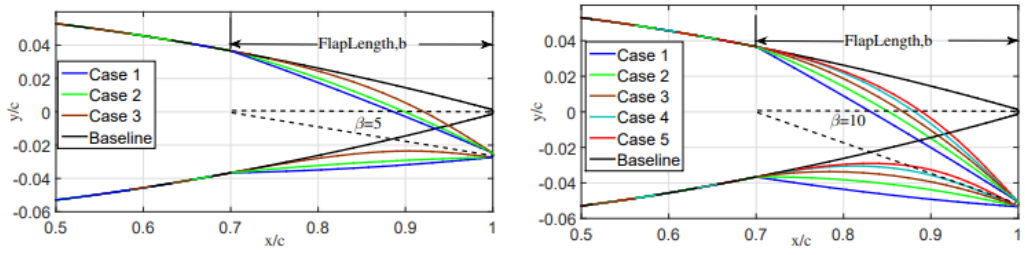

Figure 1.7: Scheme of the different trailing edges fitted in the wing used in [11].

Experimental results show an increase in the maximum value of C_L of up to 13% in the case of a highly cambered profile compared to the hinged flap profile just before entering stall at $\alpha = 13°$. However, for low angles of attack, the best performance was achieved with a slightly less cambered trailing edge. The overall C_D behavior of the morphing trailing edge increases with the increase in trailing edge camber profile. The angle of attack in which stall happens does not change as a result of morphing trailing edge profiles and further studies are necessary for understanding the post-stall properties and flow behavior. Results suggest that the effect of morphing profile will be even more important for larger deflection angles, requiring more investigation.

Detailed flow field measurements at downstream wake locations were performed using hot-wire anemometry and then compared with CFD results. Data showed that the highly cambered case had a larger flow deflection angle and slightly higher velocity deficit. This flow behavior corresponds to the separation and recirculation observed on the pressure side of the highly cambered case. Results also have shown a favorable delayed separation on the suction side of the highly cambered configuration, but an unfavorable early separation on the pressure side, which is not present when having a simple hinge flap.

It was concluded that, in order to achieve optimum aerodynamic performance with delayed flow separation on both sides, the camber of both the upper and lower surface would have to be morphed independently of each other.

The same experimental setup was used by Jawahar et al. [28, 34, 35] in a collaborative work regarding the same topic. A series of papers were published using the same wing and concept, in which diverse experiments are described. These were used to further understand the aerodynamic, aeroacoustic, and wake turbulence characteristics.

Lift and drag were measured using a force platform. It was observed a better overall lift performance for the morphed airfoil compared to the hinged one, showing an increase of up to 14%. The stall angle of both airfoils remains unchanged, which is consistent with the results in the literature. The drag coefficient values show a trend for lower results in the case of the hinged flap. The lift-to-drag coefficient ratio results show a large difference between the hinged and morphed airfoil at low angles of attack, showing an improvement of up to 6% for the morphed airfoil, with this difference in performance decreasing as the angle of attack increases, with an insignificant benefit when $\alpha > 7°$.

The pressure distribution measurements around the airfoil were performed with pressure ports distributed over the surface of the wing. For angles of attack lesser than $4°$, a prominent difference is visible between the hinged and morphed configuration, however, it subsides as the angle of attack is increased. Prominent differences in the pressure coefficient between the two configurations can also be observed around the flap region, more notably on the suction side. Results show that even a slight change of the flap camber shape with the same deflection can substantially change the pressure distribution and the suction peak at the leading edge of the airfoil, especially at low values of α.

Surface flow visualization was achieved with an oil-flow visualization technique on both the suction and pressure sides of the airfoil to visualize the boundary layer behavior and flow separation point on the airfoil flap surfaces. Results on the pressure side did not present relevant conclusions. In contrast, on the suction side, the trailing edge flap clearly indicates that the boundary layer flow on the suction surface separates at the hinge point for every angle of attack. Meanwhile, in the morphed configuration, flow separation gradually transitions upstream from the trailing edge location towards the hinge.

The flow behavior around the airfoil and in the wake region was captured using Particle Image Velocimetry. Mean velocity results showed increased wake deficit for the morphed airfoil when compared to the hinged airfoil at the near-wake locations.

With these studies, it was concluded that the increased drag at low angles of attack can be attributed to the recirculation and increased unsteady flow behavior observed on the pressure side of the morphed airfoil that was absent in the hinged airfoil. This study demonstrates that the changes in the camber profile of the flap with the same deflection angles can have a significant impact on the aerodynamic performance of airfoils. This study also shows that an additional degree of freedom, in the form of independent movement of the upper and lower surfaces, may lead to a better aerodynamic performance of the airfoil.

In 2019, Communier et al. [36] presented another design, shown in Figure 1.8, for a morphing trailing edge wing, and compared its performance with a rigid aileron. It was intended to convert a NACA0012 airfoil into a NACA4412, attaining a significant increase in lift while incurring a small impact on drag, obtaining a higher lift-to-drag ratio. One of the main goals was to develop a mechanism that could improve aerodynamic performance without increasing the weight. The concept uses vertical incisions to enable the deformation of the trailing edge. The length, number, and width of these incisions influence the amplitude of deflection. A servo motor acts directly on the trailing edge, pulling it downwards or upwards.

Figure 1.8: Deformed rib in the design used in [36].

Initial computational analyses were performed in order to verify the effectiveness of the concept. A rigid aileron was compared to the morphing trailing edge, both with a vertical displacement corresponding to 6.8% of the chord. The chosen calculation method does not allow for the aerodynamic coefficients to be computed after the stall, stopping calculations at $\alpha = 14°$. Regarding drag, morphing generates less drag than the deployment of the aileron for the same displacement, but mainly due to the deformation of the camber taking place for a larger portion of the wing chord than the aileron. The wing with an inclined aileron generates more lift but incurs in more drag, while the morphed one generates less drag but also less lift. An evaluation of the L/D ratio shows that the inclined aileron has better performance for $\alpha < -5°$, with the morphed trailing edge presenting itself as more adequate for higher angles. These initial results provided the motivation to continue with experimental studies.

The manufactured wing has a chord of $254\,\mathrm{mm}$ and span of $292\,\mathrm{mm}$, being limited by the dimensions of a NACA0012 reference wing, which was compared to the developed one and was tested for a range of speeds. The angle of attack of the wing was changed from $-10°$ to

$20°$ and force measurements were carried out with an aerodynamic scale equipped with force sensors. An initial test with no deformation was performed to compare both wings, showing an increase in drag for the developed wing, due to the discontinuities as slits on the surface of the wing. Another wing was developed based on the reference wing, but this time with an aileron with 25% of the wing chord and $241\,\mathrm{mm}$ of span.

The results obtained in this paper have shown an improvement in the effectiveness of the morphed trailing edge on the wing drag, especially in the sections where the ailerons are located. This comparative study between the morphed and the rigid aileron has verified that both had the same behavior regarding the increase of lift with the angle of attack. However, drag analysis showed more drag being produced by the aileron. Analyses of the L/D have shown that the morphed trailing edge gave a lower drag for the same lift as an aileron, which led to less fuel consumption. As a bonus, both developed wing use the same components, a rib, and an actuator, and thus does not increase the weight of the final wing.

In the same year, Ullah et al. [37] performed a numerical and experimental evaluation of the performance of Parabolic flaps. The base of the study was a NACA0015 airfoil with five parabolic deflections, ranging from $0°$, or symmetrical, to $20°$, with the hinge position at 60% of the aerodynamic chord. In order to better compare the obtained results from both numerical and experimental studies, the conditions in which both were conducted were similar, resulting in a Reynolds number of 3.25×10^5.

In the experimental studies, the five rigid wings presented in Figure 1.9 were 3D printed with a chord of $0.2\,\mathrm{m}$ and span of $0.3\,\mathrm{m}$, limited by wind tunnel dimensions. To properly evaluate the geometries, each wing was first tested with a load cell attached to at $1/4$ chord, to determine the aerodynamic forces with small increments of the angle of attack. Then, a PIV campaign was undertaken to obtain the flow field velocity in various regions. This set allows for symmetric and cambered configurations to be examined at a baseline angle and near stall angles.

CFD analyses were performed for the same five airfoils based on the NACA0015 in conditions modeled to mimic the wind tunnel setup. NASA's FUND3D was the solver used for the analysis. A hybrid mesh was chosen so that the airfoil and surrounding mesh could be scripted to rotate to the appropriate angle of attack. The tunnel walls on top and bottom are modeled as viscous walls as well as the airfoil.

To compare the performance of the parabolic and articulated flap, a script was used to run XFOIL on this airfoil for a range of angles of attack and flap deflections, for both flap types. In terms of lift, it was shown that a parabolic flap is typically better than the articulated flap, meaning that it takes less deflection than the articulated flap to produce the same lift. Regarding drag, the obtained graphs were difficult to read, but a conclusion that was taken is that there is a region of lift coefficients where the parabolic flap has less drag and another region where the articulated flap has less drag.

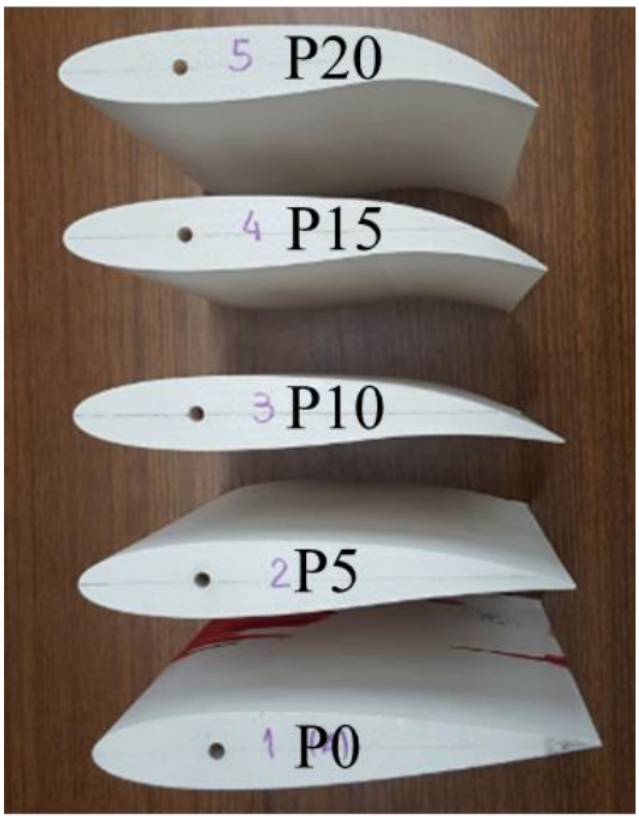

Figure 1.9: Airfoil models 3D printed used in [37].

Comparing the experimental results with the CFD results, a pattern shows that by increasing trailing edge deflection and angle of attack, the lift increases, the general shape of the drag coefficient is consistently increasing with α, and the moment coefficient also follows the expected trends, with higher deflection resulting in higher values of C_M.

Regarding flow field velocity, results demonstrate slightly higher velocity contour levels of PIV. However, the results compare favorably in all regions with the CFD. The most notable differences are being detected for the cases of high angles of attack. Important conclusions regarding the benefit of parabolic flaps are still being studied by the authors.

Alulema et al. [38] performed a study to evaluate the power consumption of the morphing wing when compared to a rigid-linked one. The base of their work was a NACA0012 wing with a compliant mechanism similar to the one presented in Figure 1.8. The numerical study consisted on the design of the wing and mechanism. Wind tunnel tests were carried out to explore the morphing capabilities and the power consumption of compliant and rigid-linked morphing wings under the effect of the aerodynamic loads, with the power required to maintain the deformed configuration also determined experimentally.

The first conclusion achieved through visualization is that both compliant and rigid-link mechanisms can produce large camber deformations, however, the first one is smoother when compared to the sharp airfoil shapes caused by abrupt surface transitions of the sec-

ond one. However, a significant difference in power consumption was encountered when comparing the power requirements. The compliant wing requires more power to deform the airfoil camber because they need energy to overcome the material resistance to deform and to overcome the aerodynamic loads, while the rigid-linked wing only requires power to overcome the aerodynamic loads. It is stated that a fatigue failure test should also be performed to evaluate the capability of the compliant mechanism.

A numerical study by Dhileep et al. [14] compares static aerodynamic characteristics of a NACA0012 airfoil that has been morphed using the single and double corrugated variable camber morphing concepts. Corrugated structures withstand large spanwise lift loads and exhibit high flexibility. The single and double corrugated structures are represented in Figure 1.10.

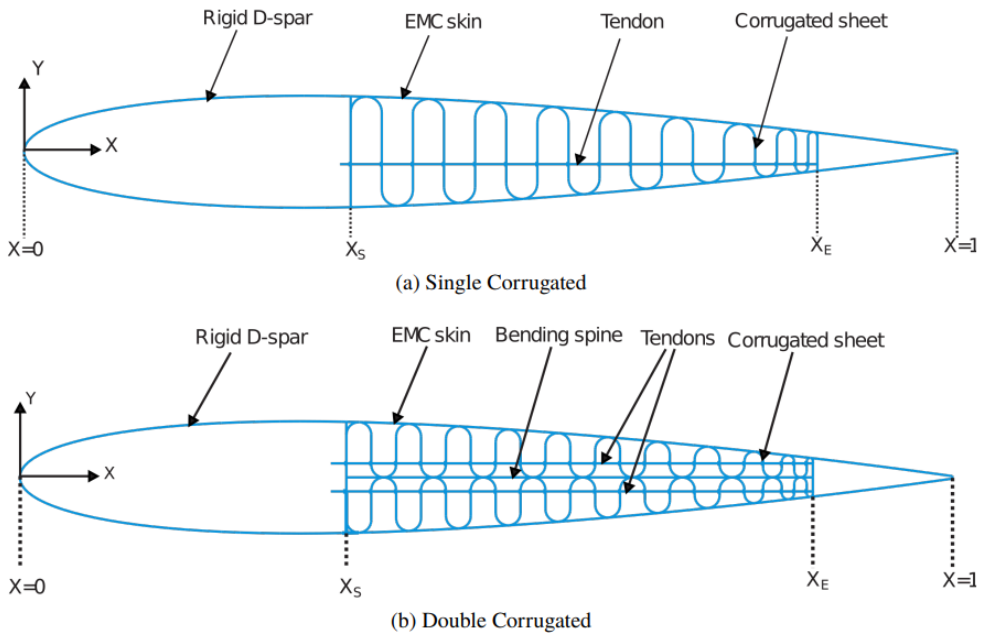

Figure 1.10: Morphing airfoil configuration used in [14].

Numerical simulations to determine the stress and deformation of both configurations were performed using the commercial finite element solver ABAQUS. In the single corrugated design, the morphing angle varies from $2°$ to $12°$, while in the double configuration, the angle varies from $1°$ to $5°$. The latter is restricted due to the wrinkling induced in the skin. To determine the aerodynamic characteristics, two CFD solvers were employed. The free stream velocity is set at $14.6\,\mathrm{m/s}$ corresponding to a Reynolds number of 10^6.

When low C_L values are required, a non-morphed airfoil performs better than morphed airfoils. When the C_L requirements become progressively higher, the morphed airfoils exhibit superior performance when compared to the baseline airfoil. Another conclusion is that single and double-corrugated variable camber airfoils demonstrate almost identical aerodynamic characteristics for a certain morphing angle, showing that the chosen mechanism depends on the constraints and requirements of the project.

As the deflection angle increases, the suction pressure over the airfoil also correspondingly increases. This results in larger lift generation along with an increase in L/D. However, the L/D reaches a peak when the morphing angle is $8°$, and then starts decreasing with an increase in morphing angle. A small recirculation region begins to develop near the trailing edge of the airfoil due to flow separation. Increasing the morphing angle displaces the separation point further upstream resulting in a larger recirculation region. This shows that an ideal value of camber may exist that maximizes the aerodynamic efficiency for any angle of attack since higher morphing angles induce flow separation that can offset the gain in lift when compared to lesser morphing angles.

Another numerical study was performed in 2021 by Majid and Jo [39]. Their main goal was to validate the aerodynamic performance and benefits of variable camber rate morphing wings when compared to conventional flapped ones. The used software to assess the behavior of the fluid around a 2D airfoil was ANSYS Fluent, in order to obtain the values of lift and drag. The velocity, fluid density, and parameters of viscosity were selected so that a Reynolds number of 7.7×10^4 was used, in order to compare the performance of camber morphing and conventional flaps in actual flight conditions of a small Unmanned Aerial Vehicle.

The studied airfoils were based on the NACA 4-digit series. The position of maximum camber was fixed at 40% of the chord and various rates were analyzed. In consequence, a corresponding NACA0012 airfoil with a flap joint at 70% of the chord was constantly deflected in order to equate the curvature of the morphing airfoil and allow for the comparison of both. CFD simulations were run for a range of angles of attack of $0° < \alpha < 15°$, with the plots of C_L and C_D being obtained.

The first conclusion was that the morphing wing results in less drag than the conventional wing while maintaining other aerodynamic parameters such as lift, that directly relate to L/D. The equivalent amount of lift generated between similar configurations is visible for every case before stall happens. However, the plots of drag show lower values for the morphing case, being more notable for higher values of camber. Furthermore, it has been found that variable camber wings equivalent to conventional aircraft wings with varying deflection flap have an improved L/D of up to 18.7%.

Whereas all morphed configurations stall at a higher angle of attack than the baseline configuration, flapped airfoils have the stall angle at lower values than the baseline configuration, meaning that morphing wings improve maneuverability and agility due to achieving a higher stall angle. This trend of a decreasing stall angle as the camber rate increases is to be expected since as the camber of the airfoil increases, the geometric change creates a suction peak on the upper surface near the leading edge that leads to an easier onset of boundary layer separation.

An experimental study conducted by Li et al. [40] was performed in order to design and evaluate a leading edge of variable camber with concentrated flexibility. The developed wing has

a chord of $410\,\mathrm{mm}$ and span of $3000\,\mathrm{mm}$, with mechanisms every $500\,\mathrm{mm}$. The leading-edge skin is crimped into an original airfoil which is then deformed to the target state under the internal mechanism's action, meaning it needs to be very flexible and robust. The bending angle is defined as the angle between the wing spar's midpoint and the maximum skin curvature point before and after the deformation. In the driving mechanism of the leading edge, each driving rib is composed of a geared five-bar mechanism. The mechanism is shown in Figure 1.11. The deformation of the leading edge can be accurately achieved by controlling the rotations of the motor.

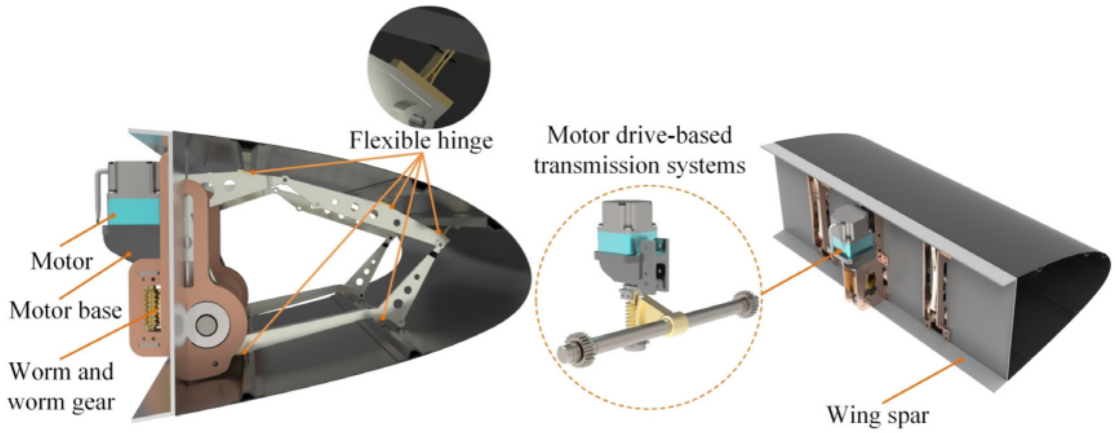

Figure 1.11: Model of variable camber leading edge used in [40].

Initially, deformation experiments were performed to visualize if the obtained shape with the deformation, as well as the final shape after, correspond to the estimated numerical results. A motion capture system is applied to collect the shape data of the skin. It can be seen that the final shape is close to the theoretical curve but the shape of the tip and lower skin is subtly different from the target airfoil.

Regarding aerodynamic characteristics, for angles of attack greater than $-3°$, the morphed airfoil's lift coefficient is significantly greater than that of the original airfoil. The original airfoil also shows higher values of drag than the morphed one. With these results, is it also visible that C_L/C_D of the morphed airfoil is higher and achieved for a smaller α than for the case of the original rigid airfoil.

Furthermore, an investigation of the airflow around the airfoil was performed. For low angles of attack, the two airfoils' surface airflow distribution is similar, with a smooth flow in the upper surface of the wing in both cases. When the angle of attack increases, the two airfoils' pressure does not change significantly, but airflow separation begins to appear in the unmorphed case. For angles greater than $20°$, the pressure distribution is uneven, flow separation increases, and moves upstream. However, at the same angle of attack, the pressure and airflow distribution on the flexible airfoil suction surface are relatively uniform, showing that this leading-edge design can inhibit flow separation and vortex formation, delay the transition of the boundary layer and also stall.

A variable camber morphing wing using a deployable scissor structure was proposed by Choi and Yun [41]. This internal mechanism is designed using the deployable structure to form various airfoil shapes through an optimization process to form the targeted airfoils with various cambers. All the airfoils have the same length of chord line and are based on the NACA 4-digit series with the position of maximum camber at 40% of the chord. Their design is presented in Figure 1.12.

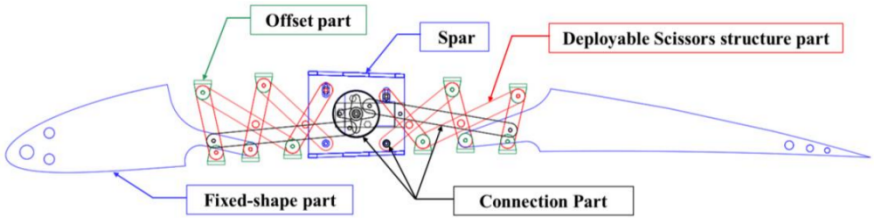

Figure 1.12: Design and parts of the variable camber morphing wing rib used in [41].

The designed morphing wing is manufactured with stainless wrench bolts, plywood, and a servo motor operating as the rotating actuator. The thickness and width of scissors members were set to the minimum value that can insert a rotary joint so that it can be manufactured lightly and operated without much effort. The developed wing is composed of ten ribs and has a span of $1.1\,\mathrm{m}$.

This paper concludes that the ribs and morphing mechanism can accurately achieve the targeted airfoil shapes with different cambers and constant chord lengths, resulting in a morphing wing with a single control variable, angle, which is defined by the position of the servo shaft. As the wing structure was performed successfully, the skin to cover the wing will be planned, designed, and fabricated in the future, using a suitable material or a structural method for deformation. Further studies for optimization of the structure and aerodynamic evaluation of the same will also be conducted.

The Fish Bone Active Camber (FishBAC) device is one of the most promising concepts in terms of both manufacturability and aerodynamic performance. The first generation was mainly 3D printed with ABS (Acrylonitrile Butadiene Styrene) plastic, and a silicone pretensioned elastomer skin was then bonded to the central structure [42]. The second generation incorporated carbon fiber composites in the spine, improving material properties when compared to 3D-printed plastics [43]. Rivero et al. have been studying the concept throughout the years [44], in which they designed, manufactured and wind tunnel tested a modular FishBAC wing with Novel 3D Printed skins. Figure 1.13 shows the second generation of the proposed concept, as well as the incorporated mechanisms for it to properly morph.

A NACA23012 airfoil with $270\,\mathrm{mm}$ of chord was selected, in which the FishBAC device is located in the rear 25% of the airfoil section, meaning that the front section is rigid and robust enough to withstand the maximum test speed. The desired tests are quasi-2D, meaning that the wing span coincides with the tunnel test section width. The five main components of the wing are: a carbon fiber reinforced composite spine, a series of spanwise stingers, two skin

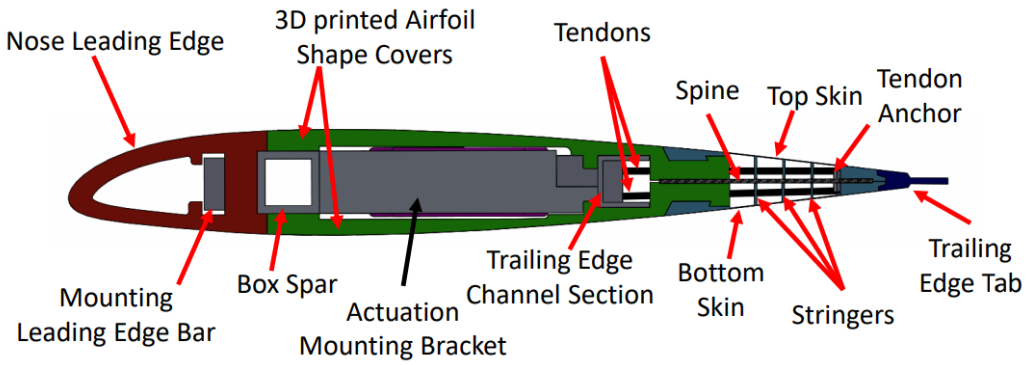

Figure 1.13: 2D profile of FishBAC wind tunnel wing model used in [44].

surfaces, a tendon anchor made of two aluminum alloy parts, and a trailing-edge tab. The actuation is provided by a high torque brushless digital servo motor in which an excellent stiffness and strength rope used as a tendon is attached. A series of support structures are developed in the rigid section of the airfoil in order to allocate every component and assure its correct operation. The motion of the servo is then reflected in upward and downward motion of the trailing edge. A series of tests were performed in order to evaluate the materials used in the construction of the wing. The benchtop proof load and static actuation tests demonstrated the robustness of both the morphing device and the actuation mechanism.

This design is very complex and time-consuming, making it difficult to replicate. However, after some comprehensive wind tunnel tests performed with this design, aerodynamic benefits were obtained.

The main goal of the wind tunnel tests was to verify if the FishBAC wing can resist the different aerodynamic loads and also to evaluate its performance and ability to generate changes in lift with a varying camber. Two 6-axis force sensors were used to measure the aerodynamic forces and moments acting on the wing, with two load cells being required to fix the demonstrator at both ends of the wing and obtain 2D aerodynamic coefficients. All measurements were conducted at $Re \approx 5.4 \times 10^5$, with trailing edge deflection ranging from $-20°$ to $40°$.

Analyzing the results, each increment in the actuation input angle generates a substantial change in the lift coefficient. For angles of attack less than $10°$, an increment up to 0.55 in the lift coefficient is measured and about 0.4 at around stall when compared to an unmorphed wing condition. The point of minimum drag shifts with the increase in camber, but it is worth noting that these drag coefficient results vary significantly with the angle of attack, which suggest that 3D effects might have been introduced in the measurements. Two-dimensional drag coefficients should remain relatively unchanged with increasing pitch angle and then abruptly change as the flow starts to separate and stall. Nevertheless, the minimum value of C_D is constant, meaning that the change in camber is essentially shifting the drag curves left and right by a consistent offset in the angle of attack. Regarding pitching moment coefficients, its variation along all tests is about 0.10, which shows the potential that the concept has for use in moment-driven control surfaces.

1.3 Objectives and Outline

There are many studies being made in the biomimetics field, more specifically in the morphing area. Despite embracing an immense number of possible study cases, researchers have been focusing their attention on continuous camber line morphing. To do so, they have been performing both numerical and experimental studies to verify the improvements in aerodynamic performance when compared to conventional airfoils and wings. However, experimental studies have been shown complex to execute due to limitations on the available materials and technologies.

Many researchers are focusing on the development of new elastic materials capable of stretch and shrink to be applied in future fully morphing wings. Other researchers' main focus has been the development of the internal structures to withstand the forces created on the surfaces while being compliant enough to change the shape of the shell.

However, the main focus of this dissertation is to present the design, development, and manufacture of a cheap and simple Morphing Trailing Edge Wing through FDM (Fused Deposition Modeling) techniques to enable aerodynamic studies in wind tunnel at AEROG and DEM (Departamento de Engenharia Mecânica) of UC (Universidade de Coimbra). The final design was then tested, in which studies of the concept's aerodynamic performance and mechanism reliability were analyzed. Furthermore, a range of trailing edge deflections and angles of attack was implemented and the data was obtained and reviewed to visualize the variations in the vortex formation and in the wake of the wing, to understand the best combinations of both variables that reduce those same vortices, as well the measurement of the aerodynamic forces that are applied on the wing.

This study also reflects the continuous interest of the AEROG research group and its members in expanding the knowledge and investigation in diverse areas of biomimetics and transient aerodynamic [45, 46, 47, 48, 49, 50, 51, 52, 53, 54, 55, 56].

This dissertation is divided into five chapters, being them the Introduction, Design Process, Methodology, Results and Discussion, and finally, the Conclusions and Future Work.

The first chapter was mainly focused on introducing the concepts of biomimetics and morphing based on the literature review. Besides, the motivation and objectives that nourish this research are also made known.

In the following chapter, a detailed description of the design and development process to obtain the morphing wing is given, taking into account the entire iterative process to reach the final solution with comments on why each prototype failed and how it was revised and refined to execute its purpose correctly.

The third chapter is dedicated to the presentation and detailed description of all the exper-

imental rig components used for the study of the developed wings. In addition, the code for controlling the wing is presented with commentaries on the behavior of each function, as well as the calibration graphs for the servo position, deflection angle, flow velocity, and strain-gauge balance. Finally, the results acquisition and wind tunnel specifications are explained, as well as the post-processing algorithm.

The fourth chapter includes the obtained results and their discussion. The different conditions are compiled and shown in various arrangements for different combinations of angle of attack and trailing edge deflection.

In the last chapter, the conclusions of the dissertation are presented, as well as recommendations for possible future studies that can be performed with the proposed wing.

Chapter 2

Design Process

The airfoil that served as the starting point for the design process is the NACA0012, in which some minor shape changes have been made in order to allow it to morph properly. Many configurations, thicknesses, and structure placements were tested until an acceptable and functional configuration was reached.

2.1 Continuous Surface Design

In this section, the evolution of the continuous surface designs is presented and described.

2.1.1 MK1

The first prototype (MK1), shown in Figure 2.1, was handmade with cardboard and wood toothpicks with a cover made of sponge. This prototype was the first approach to the concept of morphing in the AEROG lab. It aimed for leading and trailing edge morphing, having a moving part on both edges and a rigid section in between. This prototype is just a proof of concept and was never considered a plausible solution due to the massive irregularity in the surface of the airfoil and the sharp angles in the hinge sections.

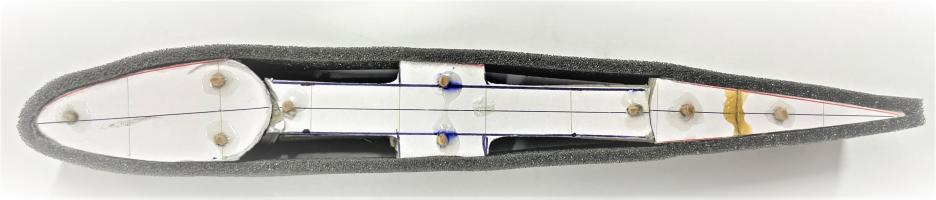

Figure 2.1: Lateral view of the MK1 design.

2.1.2 MK2

The second prototype (MK2) was an iteration of the first one but using FDM, in which a 3D model of the external surface with a $1.2\,\mathrm{mm}$ thickness of the wing was designed using the SolidWorks software.

Most prototypes were initially tested at a smaller scale, so that time and material could be saved in each prototype's printing. Both the leading and trailing edges had a small semi-circumference, as represented in Figure 2.2, in which an actuator arm would be attached. This arm was connected to a servo in the middle of the wing that would pull the edges towards the middle to deflect them downwards. This design was discarded due to warping of the lower surface of the wing.

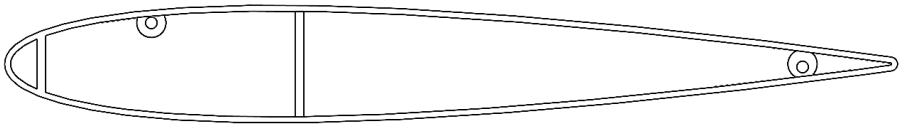

Figure 2.2: Lateral view of the MK2 design.

2.1.3 MK3

In the third prototype (MK3), which can be seen in Figure 2.3, a similar approach was used, but instead of 3D printing with PLA (Polylactic acid) filament, the material used was Nylon due to its greater flexibility. However, Nylon proved itself to be a tricky material to 3D print, and the results were unsuccessful since bumps kept appearing on the outer skin due to warping in the lower camber.

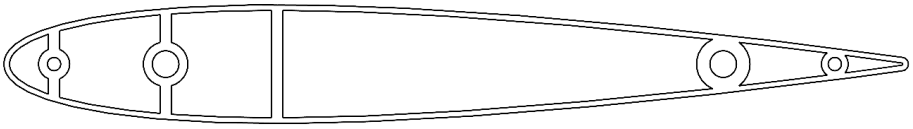

Figure 2.3: Lateral view of the MK3 design.

Therefore, the use of Nylon was discarded for the subsequent developments, returning to PLA. Another method for leading and trailing edge rotation was also tried. After some tests, a cut was performed on the skin, creating a small gap in which the excess material could slide through to the interior of the airfoil, as shown in the following subsection. After this small adjustment, a smoother curvature in both the upper and lower camber could be achieved since the problems created by warping were reduced.

All the following developments were designed and developed considering this small gap in the lower surface. Another detail that was considered for the rest of the development phase was that, in order to allocate the servo motors and actuator mechanisms inside the final wing, the airfoil chord should be around $20\,\mathrm{cm}$.

2.2 Sliding Surface Design

In this section, the evolution of the sliding surface designs is presented and described.

2.2.1 MK4

The fourth prototype (MK4) was the first of the developments to be thought and designed considering the discontinuity in the lower surface of the wing and it is represented in Figure 2.4.

As stated previously, this discontinuity is essential for the wing to morph properly with a smooth surface without warping, which would interfere with the flow. Another consideration that was taken into account was only to morph the trailing edge, which reduces the complexity of a double-morphing wing. Although it is a simpler design, there are still interesting studies to be performed, such as the comparison between a standard flapped wing *versus* a morphing trailing edge wing.

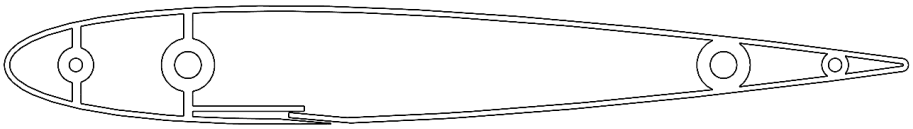

Figure 2.4: Lateral view of the MK4 design.

In this design, the wing morphs by the action of a sliding tongue that is pushed to a cavity inside the wing through a small ramp created on the skin where the discontinuity is located. So, a pull on the sliding tongue is translated into a downward deflection of the trailing edge with a smooth camber in the lower surface of the wing. However, the discontinuity in the surface might have an influence on the flow around the wing. Therefore, research for an elastic material to act as the outer skin was made in order to enable a smooth, plain, and continuous surface of the wing, regardless of the deflection imposed on the trailing edge.

The chosen material was high-density lycra that is applied on the wing when deflection is maximum. Tests show us that this extensible material allows for continuous surface morphing without bumps or gaps in the surface. Later on, it was discovered that the gap in the lower surface does not have a significant impact on the visualization of the flow around the wing, so the outer skin was discarded.

This design was discarded due to the simplicity of the interior structures of the wing not allowing for a uniform morphing of the trailing edge. The same deflection imposed on the trailing edge could result in different deformations of the airfoil, and the relative thickness was very irregular too. Therefore, new updates and structures inside the wing needed to be reconsidered.

2.2.2 MK5

As shown in Figure 2.5, the fifth design (MK5) brought the addition of a trailing edge structure similar to the ARCS (Airfoil Recambering Compliant System) geometry used in [57] to allow a parabolic deflection and uniformity across the various tests.

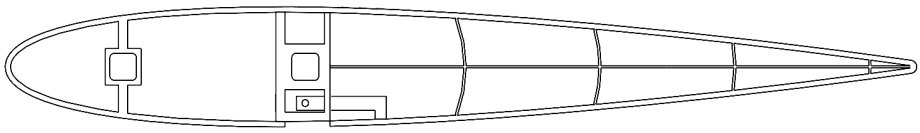

Figure 2.5: Lateral view of the MK5 design.

Two structures were added in the front part of the wing to ensure that the leading edge retains its form independently of the deflection but also to allow for stabilization and fixation of the wing once the wind tunnel tests begin.

The rear structure was placed in the desired hinge point for morphing and shaped taking into account the sliding action of the trailing edge. The front structure is placed at a distance that allows for the servo to be inserted inside the wing and between structures. Both of them have a hole where the fixation stringers will pass through, holding the wing in place while the experimental tests are performed.

The ramp structure in the lower camber was replaced by a small gap. To perform the sliding movements of the trailing edge lower camber, an L-shaped actuator was added so that the rotating movements of the servo could be converted into push and pull movements of the skin and consequently in deflections of the trailing edge. To allow the actuator to move forward, a slot was created, through which it smoothly slides while forcing the lower surface against the structure to ensure both the fixed and moving parts are at the same vertical position.

2.2.3 MK6

A radical change was attempted in the following design (MK6), in which a simplification of the sliding mechanism was made, represented in Figure 2.6.

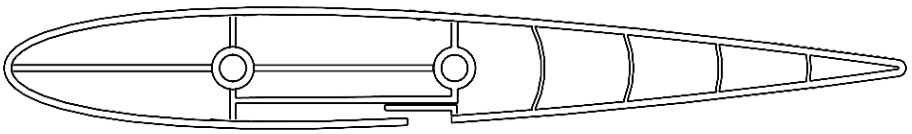

Figure 2.6: Lateral view of the MK6 design.

The actuator would not pass through the rear structure but instead, lean against a rail created between both structures. However, this mechanism did not prove itself to be robust enough to handle all the loads created by the moving section of the wing since the structure did not retain its shape, which resulted in inaccurate sliding movements of the trailing edge.

In this design, the thickness of the shell was slightly increased to guarantee the structural in-

tegrity of the leading edge. This change came with the disadvantage that the trailing edge also got stiffer and harder to morph, requiring a bigger load to deflect properly. Another drawback this change evidenced was that the arcs in the trailing edge do not allow the deflection to be uniformly distributed along this section of the wing since all the curvature is created in the section nearest to the hinge while the others retained the unmorphed NACA0012 shape.

2.2.4 MK7

The seventh design (MK7) returned to a similar concept to the MK5. As seen in Figure 2.7, some definitive changes were made, such as the arc geometries in the trailing edge being replaced by a spring-like structure similar to the one in [57], allowing for a distributed parabolic deflection of the trailing edge.

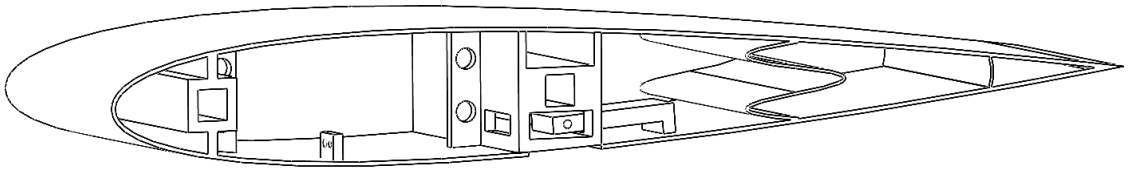

Figure 2.7: Three-dimensional view of the MK7 design.

On the lower surface, the gap was increased so that a greater section of the surface could be pulled, resulting in higher deflections of the trailing edge, increasing the range of tests that can be performed with this design. Another design change was the placement of the hinge at 50% of the chord of the airfoil, equally dividing it into a fixed front section and a rear movable one. This change was essential to allow the placement of actuators and servos inside the wing due to its dimensions.

Other changes were performed, such as a reduction of the shell's thickness to $0.8\,\mathrm{mm}$ to decrease the required load to morph but also the use of a different filament during printing.

The actuator also suffered some small adjustments. Firstly, a small hole was created in it from where a thin thread goes through and subsequently attaches to the servo arm so that motion can be applied to the actuator. Since the servo arm performs a rotary movement around the servo's center axis, the thread also passes in a small structure located inside of the lower surface, near the point where the servo arm touches the shell.

2.2.5 MK8

In the eighth design (MK8), a new mechanical design was implemented to move the lower surface of the trailing edge. Such design is shown in Figure 2.8. In order to eliminate any possible losses caused by the threads, a decision was made to create a linear actuator to pull and push the trailing edge, as shown in Figure 2.9.

To do so, a toothed gear, represented in Figure 2.10, was designed to be fitted in the servo shaft, and its rotational movement is transferred to a toothed linear actuator that is attached

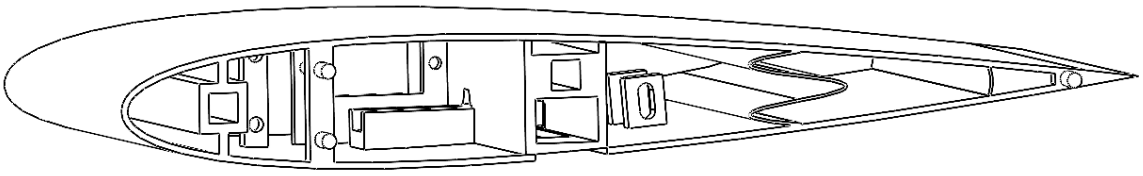

Figure 2.8: Three-dimensional view of the MK8 design.

to the surface by a structure, which is the same length of the gap in the lower surface.

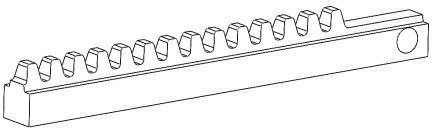

Figure 2.9: Actuator designed for the MK8 design.

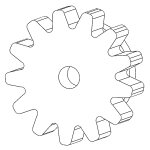

Figure 2.10: Gear designed for the MK8 design.

Maximum deflection is reached when the actuator is fully pulled, coinciding with a $180°$ rotation of the servo. In the non-toothed section of the actuator, a hole is located to allow for a screw to pass through and attach the actuator to the trailing edge strut. That strut has an ellipse-shaped hole to allow small vertical movements of the screw in order to ensure the correct distance between the fixed structure and the sliding surface while avoiding the accumulation of tensions and plastic deformation of it. This way, the trailing edge deflection is repeatable, with a smooth and continuous structure.

2.2.6 MK9

When it comes to the ninth design (MK9), which is shown in Figure 2.11, the most notable change implemented was the variable shell thickness in the front and rear sections of the wing.

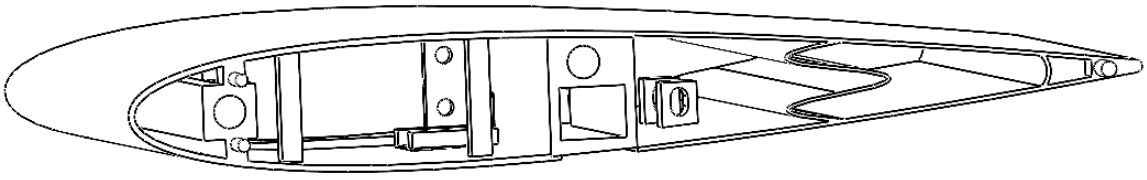

Figure 2.11: Three-dimensional view of the MK9 design.

The front section kept the $1.2\,\mathrm{mm}$ shell thickness, but the rear one was once again reduced to $0.8\,\mathrm{mm}$ due to being the mobile part, and a thinner shell requires less torque to morph correctly.

Thus, we get a rigid front section and a more flexible rear one, balancing the necessities of both parts of the wing. During testing of the previous designs, it was noticed that high torque servos would be essential for the morphing of the trailing edge since regular micro servos do not have enough torque to pull the actuator for the planned span. These high torque servos fit tight in the front section of the wing with not much space left.

This fact demanded a readjustment of the toothed linear actuator due to the servo's shaft position being restricted to a certain point. To solve this problem, the toothed section of the actuator was $3\,\mathrm{mm}$ lowered, and the gear radius was reduced to enable the mechanism to work. To compensate for the step created on the actuator, this was enlarged in order to better withstand the loads, as seen in Figs. 2.12 and 2.12. Some extra vertical stringers were added to reinforce the front section and ensure its format.

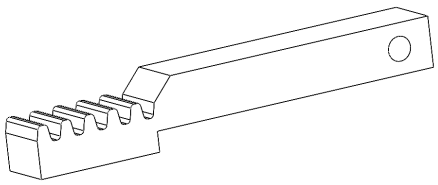

Figure 2.12: Actuator designed for the MK9 design.

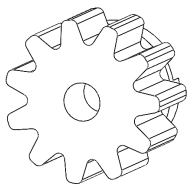

Figure 2.13: Gear designed for the MK9 design.

The MK9 was put under mechanical testing to validate the structural integrity of the system. The prototype was submitted to 2000 cycles of maximum deflection followed by a return to the original position at a $1\,\mathrm{Hz}$ frequency. However, while testing, it was noticed that the lower surface of the rear section was cracking near the structure where the actuator is attached due to the strains caused by the movement of the actuator and morphing of the trailing edge.

2.2.7 MK10.A

This region had to be reinforced in the tenth design (MK10.A), and to do it, instead of using a small screw to attach the structure to the actuator, more attaching points were added along the span, and a segment of threaded rod was used to distribute the loads of the actuator through the different structures, as seen in Figure 2.14. Furthermore, the shell thickness in that region was somewhat increased along the span. This prototype was also submitted to a stress test, having completed 4000 cycles at the same $1\,\mathrm{Hz}$ frequency without showing any indicators of cracks or defects.

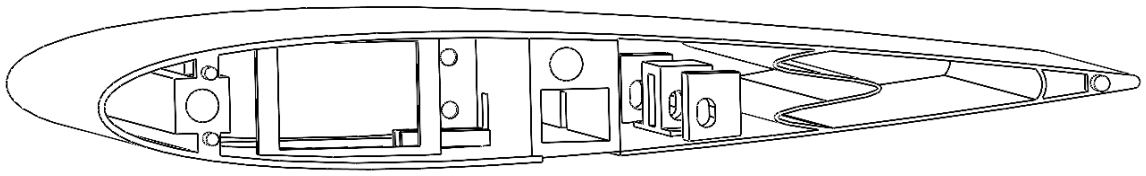

Figure 2.14: Three-dimensional view of the MK10.A design.

2.2.8 MK10.B

In order to implement this concept in the DEM-UC's wind tunnel, some adaptations were necessary to be performed on the latter design, resulting in the eleventh iteration of the concept (MK10.B).

As seen in Figure 2.15, the changes implemented on the left and mid sections were quite small compared to the MK10.A design. We can just point out that this wing section was mirrored

in order to ease the implementation of the wing in the wind tunnel, but also that a bigger gap was created in the front structure for cable management.

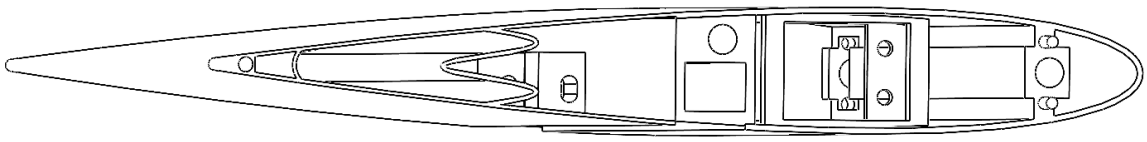

Figure 2.15: Three-dimensional view of the left and mid sections of the MK10.B design.

However, in the right section of the wing, bigger changes had to be performed, besides the ones previously described for the left and middle sections. Since the aerodynamic scale is mounted on the right of the tunnel, and its fixation to the wing is accomplished by a single $12\,\mathrm{mm}$ circular axle, a structure inside the wing was developed to fixate this axle. This section is located in the aerodynamic center of the airfoil, at $1/4$ of the chord, i.e., $50\,\mathrm{mm}$ from the leading edge of the wing. We can visualize in Figure 2.16 that a structure with thick walls is located in the furthest most right part of both this section and has a $12\,\mathrm{mm}$ hole inside that is $40\,\mathrm{mm}$ deep in which the axle tight fits.

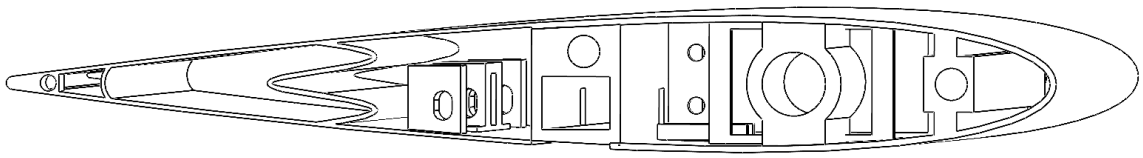

Figure 2.16: Three-dimensional view of the right section of the MK10.B design.

Having the axle on the right side of the wing was the reason why the sections had to be mirrored because, in previous designs, the servos were mounted in this part of the section. In this design, they are implemented in the left part of each section, near the gap for cable management.

Furthermore, a small cover, represented in Figure 2.17, was developed to fit in the front part of each end of the wing.

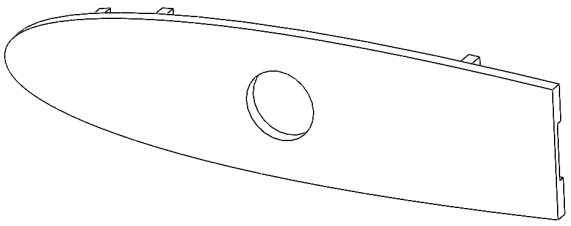

Figure 2.17: Three-dimensional view of the cover placed at each end of the wing.

Chapter 3

Methodology

The main purpose of this chapter is to present and explain detailed information about the designed wings and experimental rigs in which each was implemented.

3.1 Flow Visualization

This first subsection is referent to the wing and rig used in the AEROG lab to perform the flow visualization tests.

3.1.1 Wing MK10.A

The manufactured wing uses the NACA0012 airfoil with a $20\,\mathrm{cm}$ chord. The hinge point is located at 50% of the chord. The mounting points are positioned $20\,\mathrm{mm}$ and $90\,\mathrm{mm}$ from the leading edge having a diameter of $6\,\mathrm{mm}$ to allow for the mounting beams to be settled. It is possible to see in Figure 3.1 that the front point is centered, but the rear one is $6\,\mathrm{mm}$ above the centerline to allow for the moving components to slide correctly.

In the morphing section of the wing, a spring-shaped structure is placed $140\,\mathrm{mm}$ away from the leading edge, connecting the upper and lower surfaces. This spring provides elastic connections which constrain deflections to conform the camber line to a parabolic shape while maintaining local thickness [57].

At half span, the structures for the linear actuator to slide and attach to both the servo and the trailing edge were placed. The structure for placement of the servo inside the wing was designed according to its geometry, and the location is defined by the constraint of both the airfoil and output shaft. In the rear section, as well as the center structure where the linear actuator is attached, two more were added $55\,\mathrm{mm}$ apart for both sides to assure structural integrity and uniform deflection, as depicted in Figure 3.2.

It can be seen in Figure 3.3 that additional supports were added in the non-morphing section of the wing to ensure the relative thickness of the airfoil at all moments. Small mounting supports were also placed on both leading and trailing edges to facilitate the joint of multiple sections to increase the final span if needed. However, analyzing the resources available at AEROG, the wing tested is composed of two sections, resulting in a wingspan of $30\,\mathrm{cm}$. These sections were held together by aluminum rods.

To manufacture the wing, a Prusa i3 MK3S+ 3D printer available at the lab was used. The

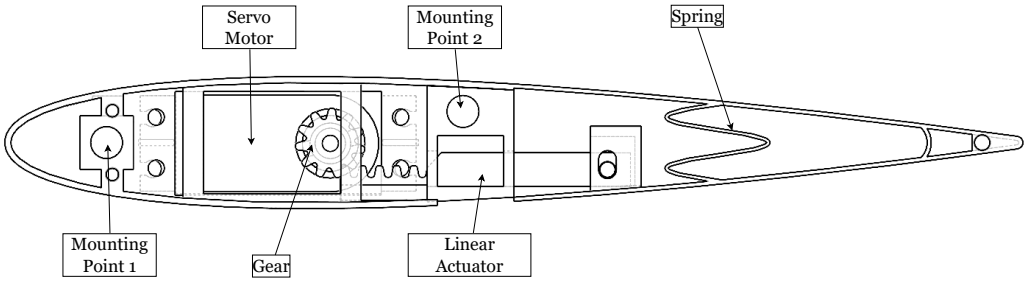

Figure 3.1: Lateral view of the final MK10.A design.

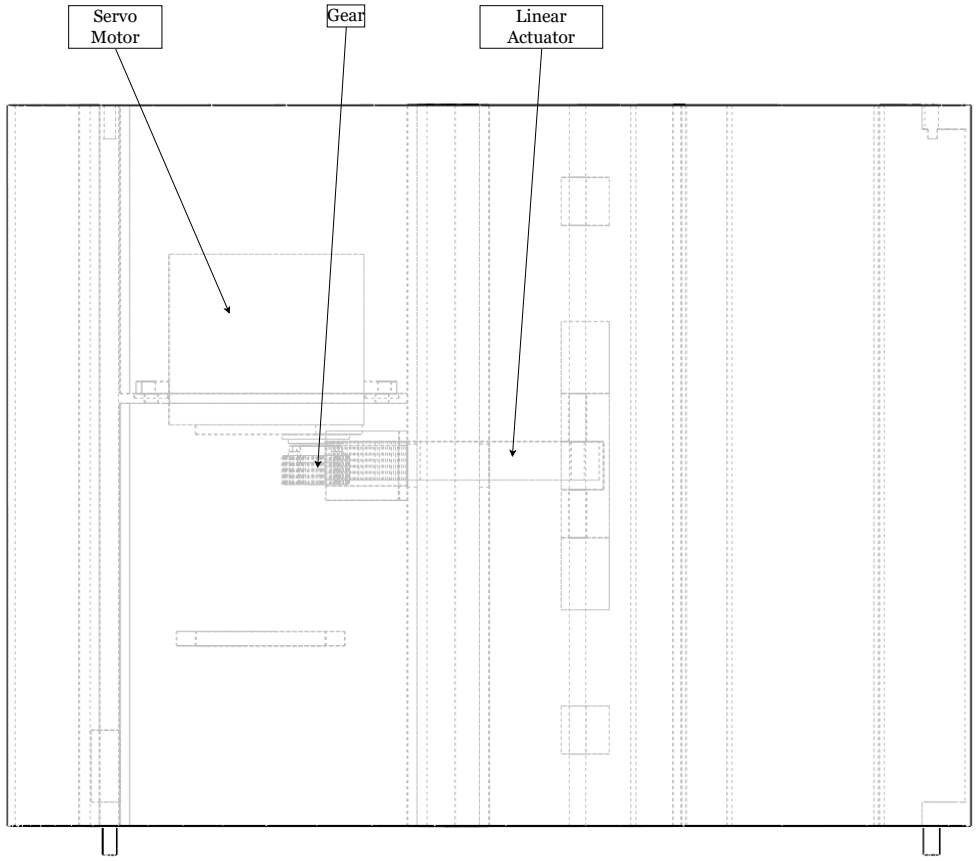

Figure 3.2: Top view of the final MK10.A design.

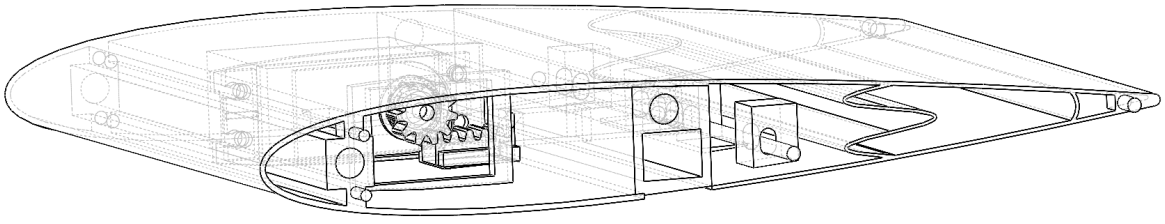

Figure 3.3: Three-dimensional view of the final MK10.A design.

chosen filament was Prusament PLA, with each section needing $20\,\mathrm{h}$ to complete the printing process, both shown in Figure 3.4.

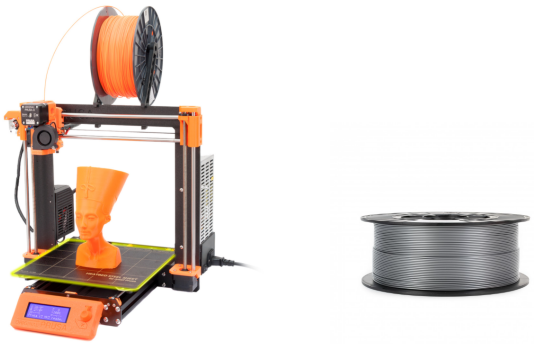

Figure 3.4: Prusa i3 MK3S+ and PLA filament.

3.1.1.1 Linear Actuator and Gear

The actuator is $57\,\mathrm{mm}$ long by $8\,\mathrm{mm}$ wide. The toothed section has a length of $17\,\mathrm{mm}$ and is $3\,\mathrm{mm}$ lower than the rest of the component due to restrictions on the positioning of the servo shaft located inside the wing. The length of the actuator was also delimited by the dimension and positioning of the support structures of the front section of the wing. A longer actuator could not be inserted inside the wing, and a shorter actuator could not fully push the lower surface forward, resulting in less trailing edge deflection.

The gear has a diameter of $14\,\mathrm{mm}$ and is composed of 11 identical and equally distributed teeth. The center section has an $8\,\mathrm{mm}$ cavity in which a universal servo adapter is glued, thus enabling the correct assembly of the gear on the servo shaft. A small screw is then used to ensure the proper fitting. Both these components were also 3D-printed in PLA in the Prusa i3 MK3S+ printer with 100% infill.

3.1.1.2 Servo Motor

The servo, shown in Figure 3.5, is an SRT DL3017 whose dimensions are $40.7 \times 20.5 \times 39.5\mathrm{mm}$, weighing $63\,\mathrm{g}$ and producing a $15.5\,\mathrm{kg\,cm}$ torque when powered by a $4.8\,\mathrm{V}$ voltage source, meaning it can be powered by the output pins of an Arduino board or similar.

Figure 3.5: Servo SRT DL3017.

Each span section of the wing requires an individual servo to morph it. Having two sections in the final wing resulted in two servos being used for this assembly. Both of them actuate at the same time and speed and are connected to the same board.

Assuming plain-flap deflection, the following graph that correlates the servo position, δ, with the deflection of the trailing edge, θ, was obtained and is shown in Figure 3.6. The final wing design deflection values were measured with the combination of a set square, ruler, and protractor.

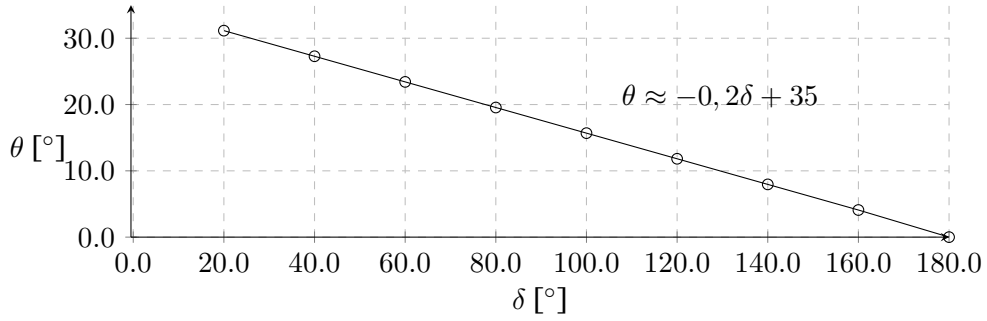

Figure 3.6: Measured trailing-edge deflection as a function of servo position for visualization tests.

The angle of attack of the airfoil can be calculated using a mathematical approximation to a plain-flap configuration. The obtained equation is:

$$\alpha \approx \alpha_0 + \arctan\left(\frac{\sin\theta}{1+\cos\theta}\right) \approx \alpha_0 + \arctan\left(\frac{\sin(-0,2\delta+35)}{1+\cos(-0,2\delta+35)}\right), \tag{3.1}$$

where α_0 is the angle of attack when the trailing edge has no deflection, θ is the trailing-edge deflection angle relative to the hinge point, and α is the angle of attack.

The comparison made in Figure 3.7 shows that the values obtained with Equation 3.1, assuming $\alpha_0 = 0°$, are quite similar to the ones measured with the combination of a set square, ruler, and protractor.

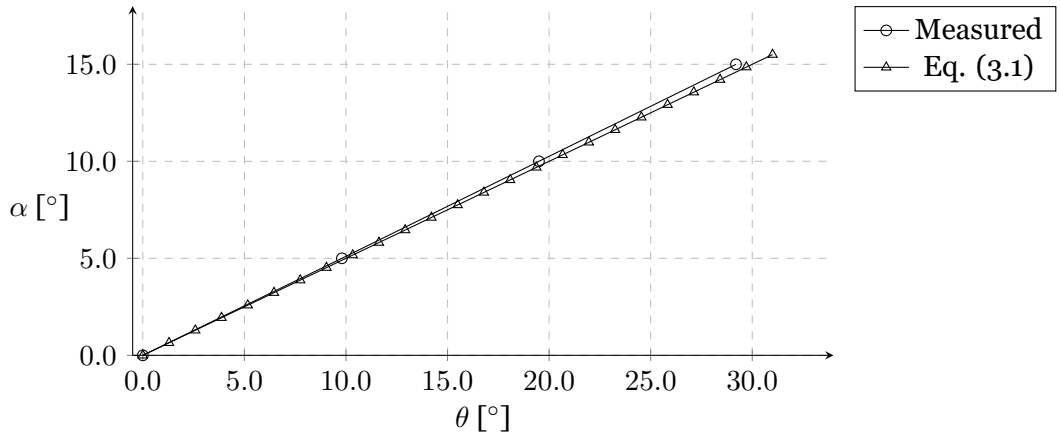

Figure 3.7: Angle of attack as a function of trailing-edge deflection for visualization tests.

These were essential in order to enable the correct programming of the microcontroller and

the repeatability of the mechanism so that the given inputs are converted in the desired deflection for each study case.

From here, it became possible to perform and compare tests for a range of angles of attack, considering only the dependency on the applied pitching angle and cases, which depends on the deflection induced in the trailing edge.

3.1.1.3 ELEGOO Mega 2560 Board

The chosen single-board microcontroller for controlling the servos is an ELEGOO Mega 2560 Arduino-compatible board that controls both servos through inputs defined by the user in a suitable 16-digit membrane keypad. Both parts are represented in Figures 3.8 and 3.9.

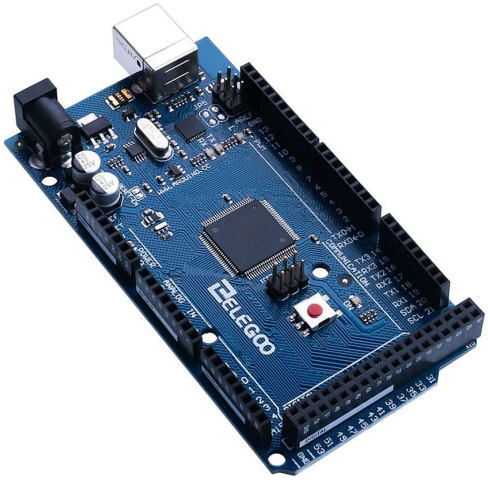

Figure 3.8: ELEGOO Mega 2560.

Figure 3.9: 16-digit membrane keypad.

The code presented in Appendix A.1 was then developed, compiled, and sent to the board.

3.1.2 Supporting Structure

As illustrated in Figure 3.10, a metal structure was developed and built to which the wing is attached. The metal structure slides on a set of rails, allowing the wing to move closer or further from the wind tunnel exit. The structure is composed of two sets of vertical components: the height of the rear one is fixed, setting the position of the rear beam of the wing at the middle of the tunnel exit; while the height of the front one is variable, using a plastic support attached to a $12\,\mathrm{mm}$ threaded rod that is screwed in a nut soldered to the base of the structure, in which the front beam is fitted. This way, it is possible to regulate the angle of attack of the wing through minor adjustments of the height of the rod, increasing the range of tests that can be performed with this structure.

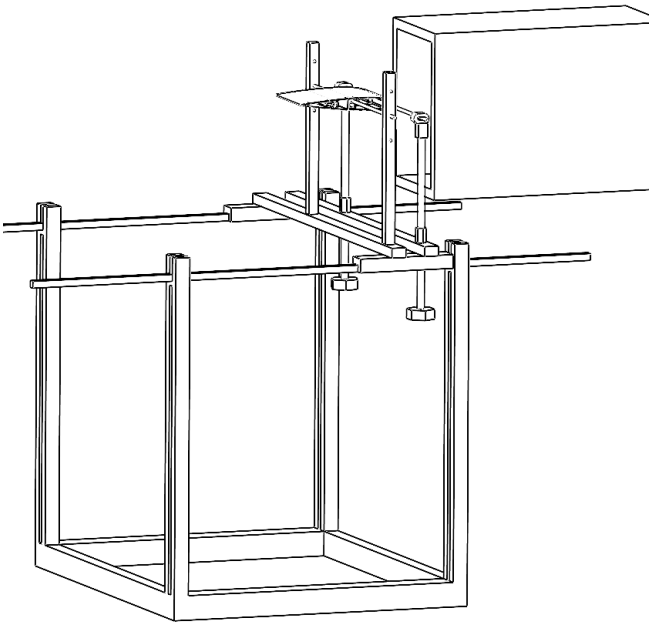

Figure 3.10: Structure used in the experimental setup.

3.1.3 Wind Tunnel

For the purpose of this study, the sliding structure was placed in a position where the leading edge of the wing is located at $2\,\mathrm{cm}$ of the tunnel exit.

Presented in Figure 3.11, the wind tunnel, developed and built in AEROG, is an open section, open circuit, and blower with a $200\,\mathrm{mm}$ x $300\,\mathrm{mm}$ exit section. It has a $15\,\mathrm{kW}$ fan that allows for a maximum flow of $3000\,\mathrm{m^3h^{-1}}$. The flow velocity is controlled by combining the opening of a guillotine located upstream and the motor frequency.

Figure 3.11: AEROG's wind tunnel.

3.1.3.1 Anemometer

In order to determine and control the flow velocity, the TSI Airflow TA410 thermal anemometer, shown in Figure 3.12, was used. The guillotine was then opened and closed according to the measured and desired velocities.

Figure 3.12: TSI Airflow TA410 thermal anemometer.

3.1.4 Smoke System

To visualize the flow around and after the wing, a smoke dispenser system was used to release particles inside the wind tunnel.

The system is composed of a TECHNO-FOG Jem thermal smoke machine, represented in Figure 3.13, vaporizing Jem Regular DJ Fluid, a water-glycerol mixture which condensates into small particles. These are then released in a controlled way through a tube located inside the tunnel so that it does not disturb the flow in a significant way.

Figure 3.13: TECHNO-FOG Jem smoke machine.

3.1.5 High-Speed Camera

Image acquisition is essential in this study, providing a better analysis of the flow around the wing and consequent wake.

To do so, a Photron FASTCAM mini UX50 high-speed camera was used. This camera provides high-resolution images (1280x1024) with frame rates of up to 2000fps. The camera

was positioned at approximately $90°$ with the flow. Opposite the camera and parallel to the flow is installed a panel of LED (Light Emitting Diode) lights, shown in Figure 3.14, with another one located above the wind tunnel's exit to brighten and highlight the smoke particles, improving the quality of the obtained images and data. The high-speed camera is illustrated in Figure 3.15.

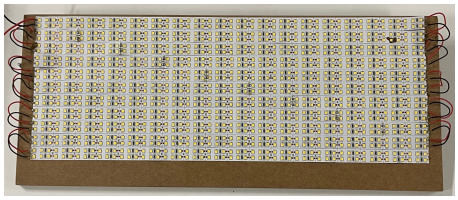

Figure 3.14: Panel of LED lights.

Figure 3.15: Photron FASTCAM mini UX50 high-speed camera.

This camera has a software to control and save the collected data, the PFV4 Photron FASTCAM Viewer.

3.1.6 Experimental Rig

All the previously mentioned elements are put together in the following way to enable the study to be performed:

1. A section of the MK10.A is 3D-printed. Inside support structures are then removed, and the outside is sanded. The actuator is inserted in the respective cavity, followed by the insertion of the servo and gear set. Respective wiring is connected to the servo, and the opposite end is placed in the cable management space inside the leading edge. The latter is repeated due to the necessity of a second section;

2. Both sections are attached together, and the aluminum rods are inserted through the defined holes. The threaded rod is then inserted through the wing structures and actuator holes, enabling the motion of the wing.

3. Wires are then connected to the microcontroller. They are connected to the port defined in the previously presented code, with VCC (Voltage Common Collector) wire connected to the $5\,\mathrm{V}$ ports and GND (Electrical Ground) to the board Ground. The same is powered through the onboard barrel jack connector using an external power supply;

4. The wing is placed in front of the tunnel exit, inserting the rods through the holes drilled in the metal structure. The pitch angle was then adjusted for the desired position;

5. The LED light panels are placed. The camera is also positioned and connected to a computer. The quality of the image is then adjusted in the software;

6. The wind tunnel is turned on. Depending on the current and desired velocity, the guillotine is opened or closed. The process is constantly repeated until the desired velocity is assured. After that, the wing can return to the initial position;

7. The smoke machine trigger is adjusted so that an ideal quantity of smoke is released;

8. The deflection of the trailing edge is selected in the keypad, and the pitch angle is adjusted with the rotation of the $12\,\mathrm{mm}$ threaded rod of the structure for the desired case. After all the previous steps, tests can start to be performed;

9. In order to correctly record the images, it is important that the camera trigger is activated only when the flow is fully developed and smoke particles are equally distributed in it. The clip is saved in the computer for further analysis;

10. Steps 8 and 9 are then repeated until every case study is performed for a certain flow velocity.

3.2 Force Measurements

This subsection is referent to the wing and rig used in the DEM-UC lab to perform the force measurement tests.

3.2.1 Wing MK10.B

The described process for the wing is similar to the one presented in Section 3.1.

The most notable change was that the new wing is composed of three sections of $15\,\mathrm{cm}$ each since the used tunnel has a cross-section that measures $45.7\,\mathrm{cm}$.

The manufactured wing is based on the NACA0012 airfoil with a $20\,\mathrm{cm}$ chord. To properly morph the airfoil, several components are added to the inner part of it, as shown in Figure 3.16.

The wing has two main spars with a diameter of $6\,\mathrm{mm}$, positioned $20\,\mathrm{mm}$ and $90\,\mathrm{mm}$ from the leading edge. The back spar is placed slightly above the centerline so the linear actuator can slide inside the airfoil with no obstruction. In the back part of the wing, a spring-shaped structure is placed $140\,\mathrm{mm}$ away from the leading edge, connecting the upper and lower surfaces. This spring provides elastic connections which constrain deflections to conform the camber line to a parabolic shape while maintaining local thickness [57].

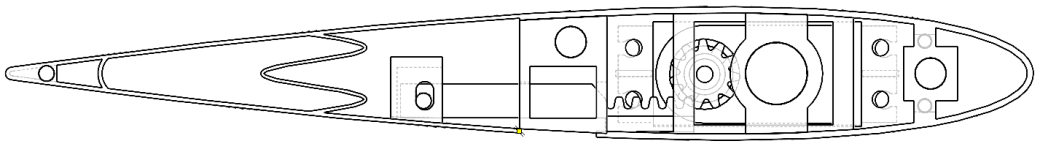

Figure 3.16: Lateral view of the final MK10.B design.

Morphing was achieved through a hinge point located at 50% of the chord, making it the pivot point of the trailing edge flap. A discontinuity in the lower surface of the wing is created so that when the trailing-edge flap is deflected, it easily sides, obtaining a smooth curvature in both the upper and lower camber. To do so, a $15\,\mathrm{mm}$ gap was created in the lower surface near the hinge point. The shell thickness in the fixed part of the wing is $1.2\,\mathrm{mm}$, being reduced to $0.8\,\mathrm{mm}$ in the movable part, reducing the required load to deform the airfoil.

The deflection of the trailing edge is enabled by a toothed linear actuator and a gear attached to the servo shaft located at the half span of the section. The rotational movement is transferred to the actuator that is attached to the surface by a central structure located on the lower surface of the trailing edge. Two more were added $55\,\mathrm{mm}$ apart for both sides to assure structural integrity and uniform deflection, as depicted in Figure 3.17.

Additional supports were added in the non-morphing section of the wing to ensure the relative thickness of the airfoil at all moments. A three-dimensional perspective of the final

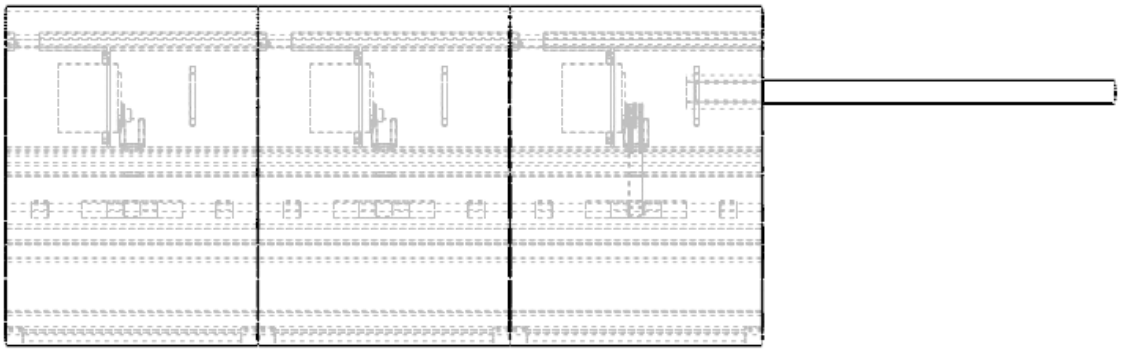

Figure 3.17: Top view of the final MK10.B design.

design is shown in Figure 3.18.

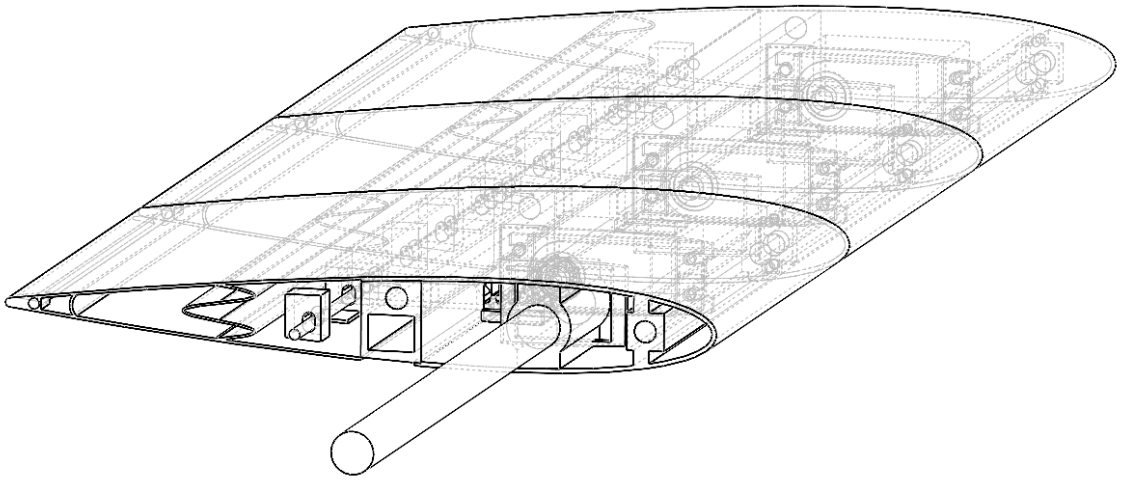

Figure 3.18: Three-dimensional view of the final MK10.B design.

The manufacturing process of the wing uses a Prusa i3 MK3S+ 3D printer with Prusament PLA filament, with each section needing approximately 20 h to complete the printing process.

3.2.1.1 Actuator and Gear

The actuator and gear used in this assembly are exactly the same as the ones described in Section 3.1.

3.2.1.2 Servo Motor

Once again, the used servo is an SRT DL3017 powered by the output pins of the microcontroller board. Due to each span section of the wing requiring an individual servo to morph it, the final wing resulted in three servos being used for this assembly. All of them act at the same time and speed and are connected to the same board.

The proposed morphing mechanism was put to test to directly link the servo shaft angle with the trailing-edge-flap deflection. In Figure 3.19, the relationship between the servo position and flap deflection is presented, assuming plain-flap deflection. The final wing design deflection values were measured with the combination of a set square, ruler, and protractor.

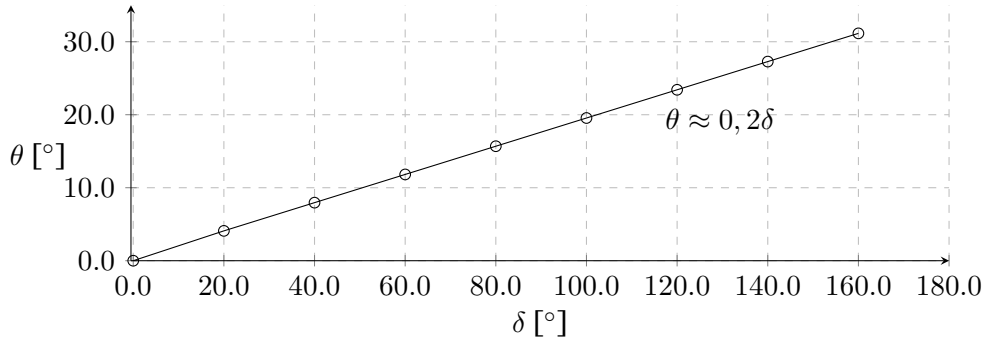

Figure 3.19: Measured trailing-edge deflection as a function of servo position for force measurement tests.

Comparing this image to the one presented in 3.1, it can be clearly seen that this slope is increasing instead of decreasing, but with the same intensity. This is due to the sections being mirrored when compared to the previous design, meaning that the rotating way is now inverted.

Similarly to what was done for the case of visualization, a mathematical approximation to a plain-flap configuration can be used to determine the angle of attack of the airfoil. This is an approximation that assumes ideal deflection. The obtained equation is:

$$\alpha \approx \alpha_0 + \arctan\left(\frac{\sin\theta}{1+\cos\theta}\right) \approx \alpha_0 + \arctan\left(\frac{\sin(0.2\delta)}{1+\cos(0.2\delta)}\right). \tag{3.2}$$

The comparison made in Figure 3.20 shows that the values obtained with Equation 3.2, assuming $\alpha_0 = 0°$, are quite similar to the ones measured with the combination of a set square, ruler, and protractor.

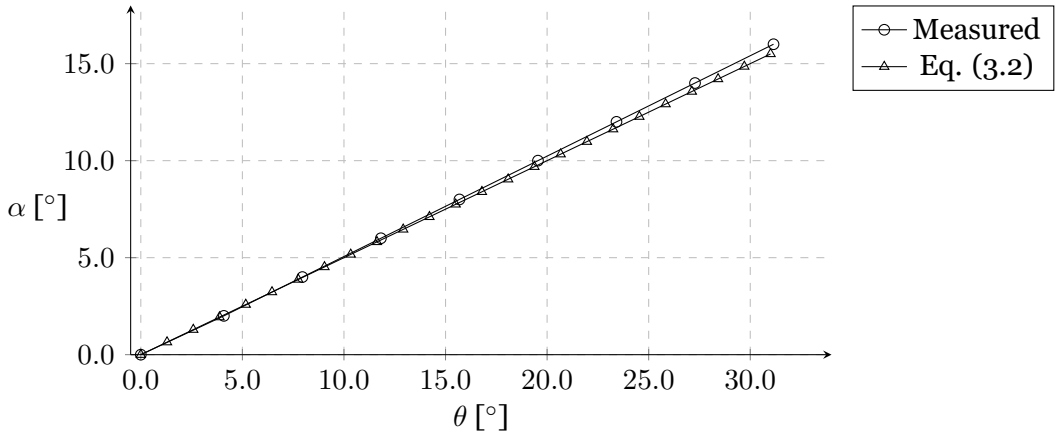

Figure 3.20: Angle of attack as a function of trailing-edge deflection for force measurement tests.

Although the slope presented in Figure 3.19 is inverted, the relation between trailing-edge deflection and angle of attack remains the same.

With these results, the correct programming of the microcontroller proceeded, with an initial verification to guarantee that the given inputs are converted in the desired deflection for each study case.

3.2.1.3 ELEGOO Mega 2560 Board

Similar to what was presented in Section 3.1, the ELEGOO Mega 2560 Arduino-compatible board and 16-digit Membrane Keypad were used to control the servos. The code had to be slightly changed before being compiled and sent to the board in order to correctly perform the new desired trailing-edge positions. The same is presented in Appendix A.2.

3.2.2 Wind Tunnel

For the purpose of this study, the wing was placed inside the closed-section testing area of the wind tunnel.

Presented in Figure 3.21, the wind tunnel in which force measurement tests are conducted is located in the Fluid Mechanics Laboratory at the Mechanical Engineering Department of the University of Coimbra. The tunnel is fabricated by Plint & Partners, having a $457 \times 457\text{mm}$ cross-section area in which experiments are performed. The fan is powered by a $14.7\,\text{kW}$ motor whose frequency can be regulated between $0\,\text{Hz}$ and $50\,\text{Hz}$, blowing the flow up until a maximum of $30\,\text{m/s}$.

Figure 3.21: Fluid Mechanics Laboratory's wind tunnel.

Being an open circuit wind tunnel, it can be assumed that the static pressure in the test section is the same as atmospheric pressure. The contraction nozzle before the test section contributes to a stable and uniform flow inside it due to a negative pressure gradient in the contraction cone, inhibiting the separation of the flow near the walls [58].

On the right side of the wind tunnel, a strain-gauge balance is coupled to enable aerodynamic force measurement.

3.2.2.1 Pitot Tube

A pitot tube was used to obtain the flow velocity for different motor frequencies through the measurement of the dynamic pressure of the undisturbed flow, the density of the fluid, and Bernoulli's equation:

$$U = \sqrt{\frac{2q}{\rho}} \tag{3.3}$$

where U is equivalent airspeed, q is the dynamic pressure, and ρ is the fluid's density.

The basic pitot is a slender tube that has two holes in it. The front hole is placed in the airstream to measure what is called stagnation pressure. The side hole measures the static pressure. By measuring the difference between these pressures, you get the dynamic pressure, which can be used to calculate airspeed. Placing the pitot in the tunnel exit, as shown in Figure 3.22, it can measure the dynamic pressure of the undisturbed stream that is going through the tunnel and present it in the digital manometer represented in Figure 3.23.

Figure 3.22: Pitot tube.

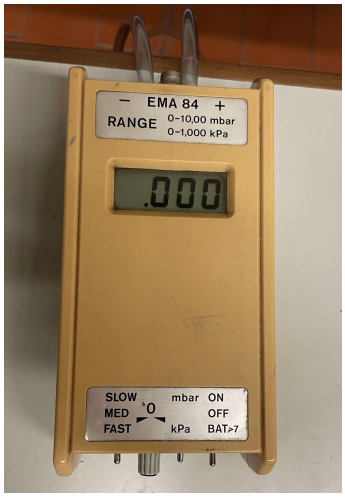

Figure 3.23: Digital manometer.

3.2.2.2 Calibration

The main goal of the calibration of the wind tunnel is to determine the relation between the motor frequency and the flow velocity. To do so, a series of frequencies were selected in the

motor control system, represented in Figure 3.24, and the corresponding dynamic pressure value was read in the manometer.

Figure 3.24: Motor frequency control system.

Considering the pressure and temperature values measured in the moment of testing, the fluid density was determined, and the flow velocity was obtained using Equation 3.3. The flow velocity, U, was then converted to true velocity, V.

The graph in Figure 3.25 was obtained:

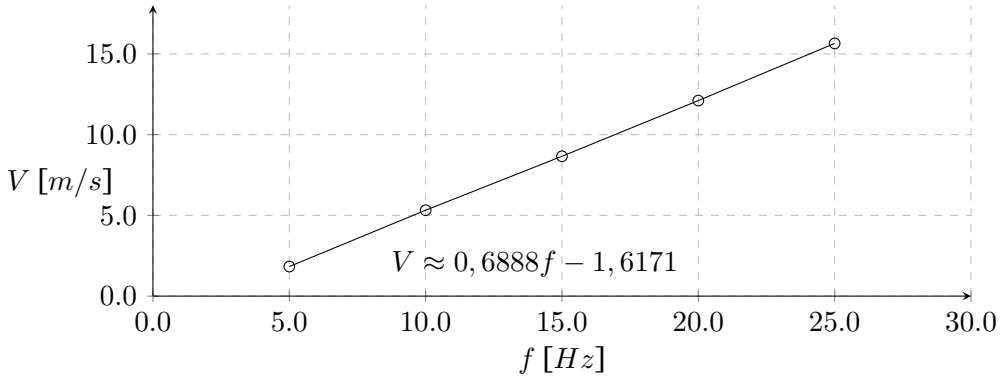

Figure 3.25: Correlation between motor frequency and flow velocity.

3.2.3 Strain-Gauge Balance

A strain gauge, represented in Figure 3.26, is a sensor whose resistance varies with the application of an external force through tensile and compressive strain, which is converted into electric resistance that can then be measured. If these gauges are allocated in carefully selected and designed locations, they can be used to correctly measure the strain produced by the aerodynamic loads. The linear characteristic of these sensors allows the use of a linear calibration slope that considerably simplifies the conversion of data provided by the sensors and its processing, using simple software.

In Figure 3.27, it can be seen the available strain-gauge balance. It has the ability to determine the horizontal and vertical components of the forces applied in the wing, as well as the moment around its axis, through the measurements in three gauges. The first gauge is responsible for the determination of the horizontal component, being then converted into

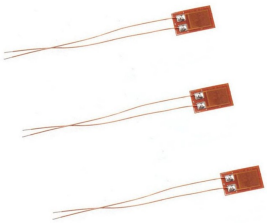

Figure 3.26: Strain-gauge sensors.

drag. The remaining two measure the values of the vertical components, being then converted into lift and moment. It is important to guarantee that all rods and springs of the balance are slightly strained and undisturbed, as well as correctly leveled, in order to obtain the best possible results.

Each sensor was connected to the analog-to-digital signal converter shown below in Figure 3.28, whose output is transmitted to a laptop via a USB cable.

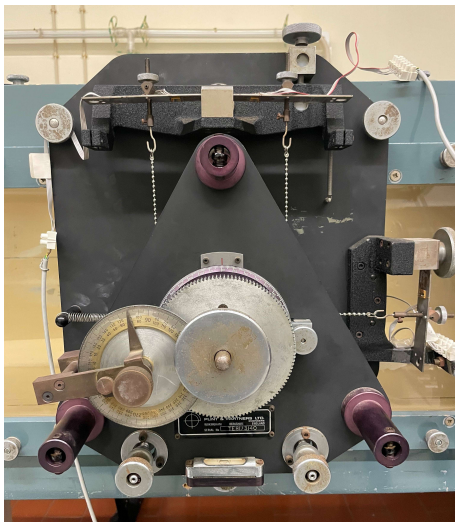

Figure 3.27: Available strain-gauge balance.

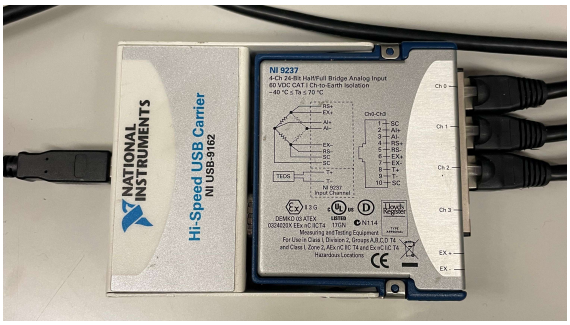

Figure 3.28: Signal converter.

3.2.3.1 Acquisition Software

The data acquisition software was developed by the Mechanical Engineering Department and was coded in LabView.

For each measurement, the program would run for 10 seconds, acquiring a total of 10000 samples and retrieving the average read value and standard deviation of each one of the three sensors, besides showing the instantaneous measured value. All the values are presented with three decimal places. The main goal of the high amount of points was to decrease the inconsistencies and errors of the signals measured in the gauges and transmitted to the software. The values presented on the screen are then transcribed to an Excel sheet. The program interface is shown in Figure 3.29.

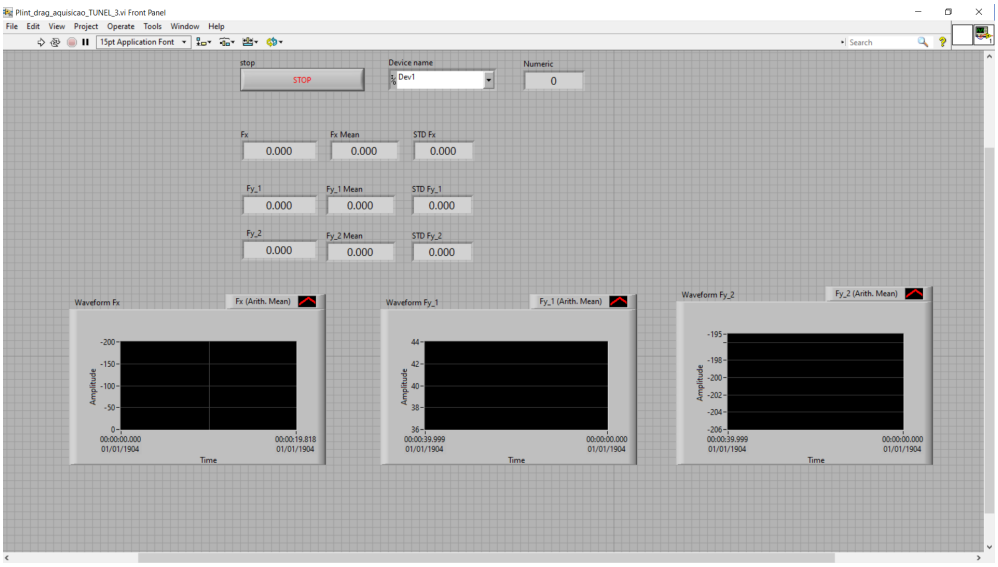

Figure 3.29: Interface of the data acquisition program.

3.2.3.2 Calibration and Data Processing

The calibration of the software was essential to establish a relation between the voltages of the strain gauges and the aerodynamic forces in the wing. To do so, in order to obtain the slope that correlates both values, a calibration rod was inserted in the balance, in which a thread of negligible mass was tied. It should be noted that during the calibration process, the wind tunnel motor was switched off.

Initially, the calibration of the two gauges of the vertical component was performed. The software was run to obtain the voltage values equivalent to no load. After that, a set of weights was used to successively increment the load in the gauges and the equivalent value in the software was registered, resulting in the calibration slopes presented in Figure 3.30.

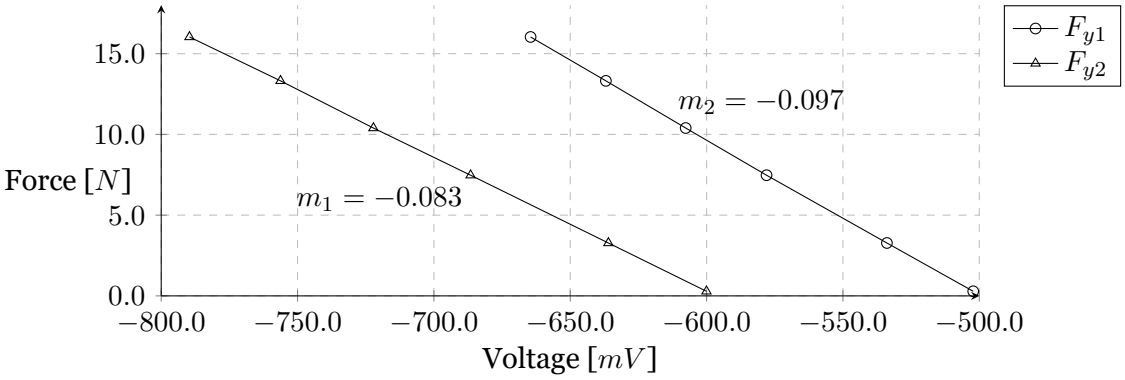

Figure 3.30: Calibration of the vertical sensors.

The slopes presented in the figure above mean that, in the sensor responsible for measuring the first element of the vertical component F_{y1}, a difference of $1\,\mathrm{mV}$ in the software translates into a force of $0.083\,\mathrm{N}$ being applied in the wing; and in the sensor responsible for measuring the second element of the vertical component F_{y2}, a difference of $1\,\mathrm{mV}$ in the software translates in a force of $0.097\,\mathrm{N}$.

The same process was then executed for the horizontal component. The main difference is that there is only one element in this component. It was important to ensure that the thread was perfectly aligned with the tunnel exit in order to guarantee that the forces applied were solely horizontal. The calibration slope for the horizontal component is presented in Figure 3.31.

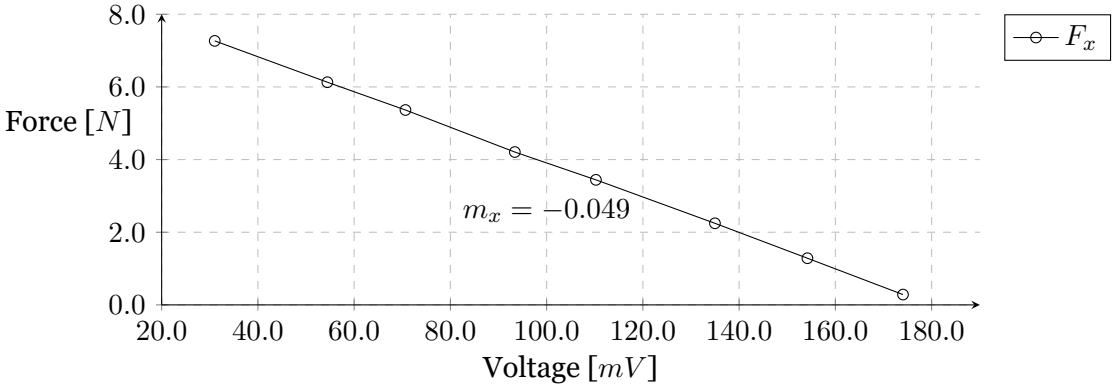

Figure 3.31: Calibration of the horizontal sensor.

The slope presented in the figure above means that, in the sensor responsible for measuring the horizontal component F_x, a difference of $1\,\mathrm{mV}$ in the software translates into a force of $0.049\,\mathrm{N}$ being applied in the wing.

It is important to refer that the presented slopes are not perfect linear equations, but all three have a coefficient of determination, R^2, above 0.9998.

In order to correctly determine the aerodynamic coefficients, the obtained values in each test need to be refined. To do so, before switching on the wind tunnel motor, it is necessary to acquire the value of the forces measured in the sensors to work as a tare weight for the values obtained with the motor working. This eliminates the effects of the own weight of the wing, as well as variation of the effects of resistance of the strain gauges.

As a result, the aerodynamic forces are calculated using the following expressions:

$$L = (F_{y1} - F_{y1,0}) + (F_{y2} - F_{y2,0}), \tag{3.4}$$

$$D = (F_x - F_{x0}), \tag{3.5}$$

$$M = [(F_{y1} - F_{y1,0}) - (F_{y2} - F_{y2,0})] \times d, \tag{3.6}$$

where L, D, and M are the lift, drag, and moment, respectively, F_{y1}, F_{y2}, and F_x are the values measured for each study case, $F_{y1,0}$, $F_{y2,0}$, and F_{x0} are the tare values obtained with no flow in the tunnel section, and d is the distance between the balance axis and the fixation points of the vertical strain gauges.

3.2.4 Experimental Rig

All the previously mentioned elements are put together in the following way to enable the study to be performed:

1. A left, middle, and right sections of the MK10.B design are 3D-printed. Inside, support structures are then removed, and the outside is sanded. The actuator is inserted in the respective cavity, followed by the insertion of the servo and gear set. Respective wiring is connected to the servo, and the opposite end is placed in the cable management space inside the leading edge.

2. The three sections are attached together and the aluminum rods are inserted through the defined holes. The threaded rod is then inserted through the wing structures and actuator holes, enabling the motion of the wing.

3. The $12\,\mathrm{mm}$ axle is then inserted and glued in the respective hole in the right section to enable wing placement in the balance.

4. Wires are then connected to the ELEGOO board. Signal wires are connected to the port defined in the previously presented code, with VCC wire connected to the 5V ports and GND to the board Ground. The same is powered through the onboard barrel jack connector using an external power supply;

5. The wing is fitted and tightened to the strain-gauge balance inside the wind tunnel.

6. The balance wiring is connected to the signal converter and then to a computer. The acquisition software is then launched, and a quick test is performed in order to verify that everything is well connected and correctly working;

7. The angle of attack was then adjusted for the desired position, as well as the deflection of the trailing edge, the latter being selected in the keypad;

8. The software is run with the tunnel off, in order to obtain the tare weight for that wing configuration. Measured values are then registered in an Excel sheet.

9. The tunnel is turned on. The motor frequency is adjusted for the desired value through the respective calibration slope.

10. After waiting for the flow to stabilize, the software is once again run in order to obtain the forces for that respective test. Measured values are then registered in an Excel sheet.

11. Steps 7 to 10 are then repeated until every case study is performed.

3.2.5 Experimental Rig Validation

In this section, the results of the lift and drag coefficients obtained for the developed wing in a NACA0012 configuration were compared with two other experimental studies for a 2D NACA0012 airfoil. The first test was performed in the same wind tunnel used in this thesis by André Bernardo, in which a solid NACA0012 wood wing was evaluated [58]. The second test was performed by Eastman N. Jacobs and Albert Sherman at Langley Memorial Aeronautical Laboratory [59]. Figures 3.32 and 3.33 show the obtained results.

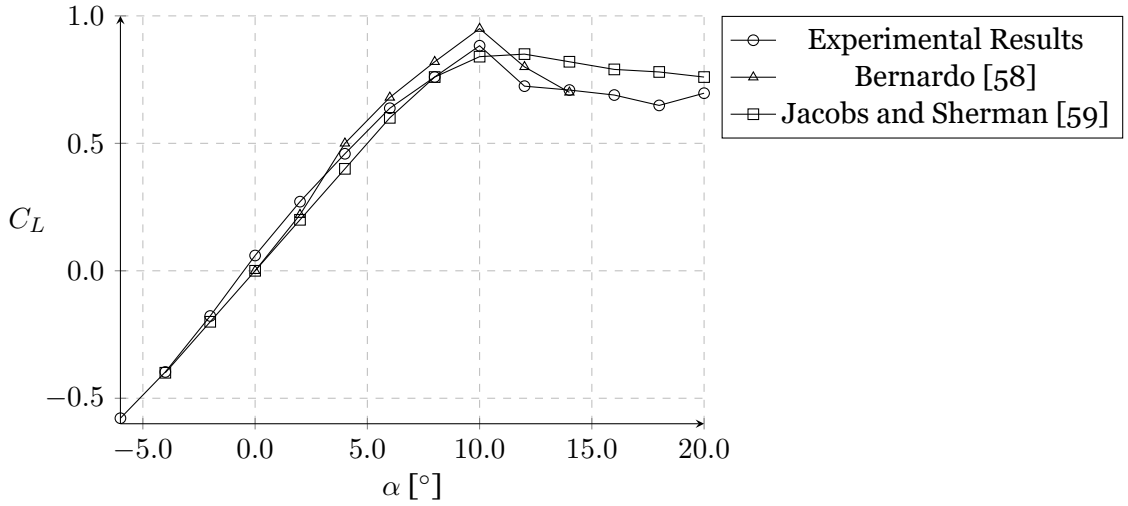

Figure 3.32: Lift coefficient comparison for a NACA0012 with infinite aspect ratio.

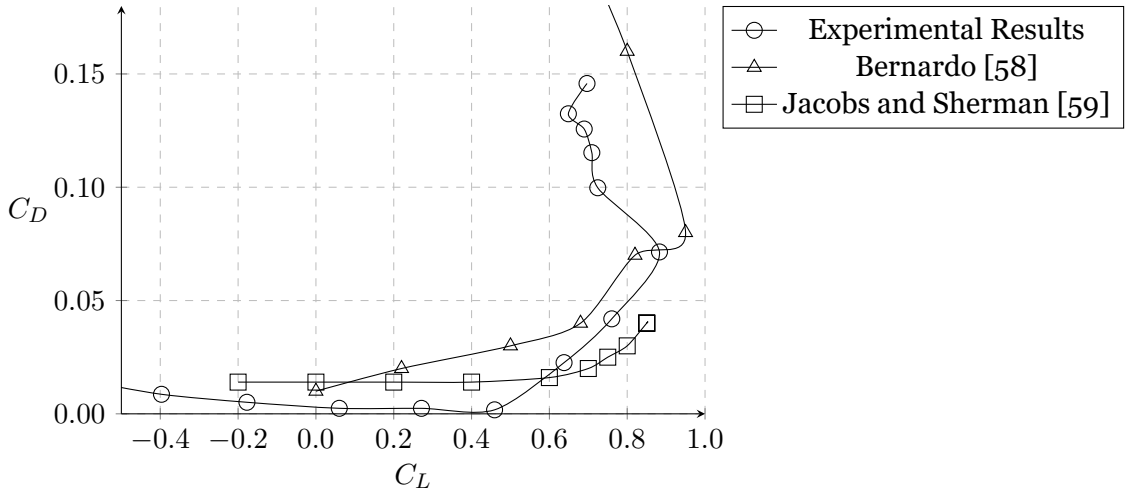

Figure 3.33: Drag coefficient comparison for a NACA0012 with infinite aspect ratio.

It can be concluded that the magnitude of the values obtained in the experimental tests concurs with the ones verified by previous sources and can be considered valid.

Although the obtained values of C_D are smaller, it is shown that the tendency of all the values compared is the same. There are a lot of reasons that can result in the differences between these values. For instance, the low loads that were measured due to the Reynolds in which tests were performed can increase measurement uncertainty. A small variation of temperature in the sensors can also affect its sensibility and result in values that are not accurate.

Chapter 4

Results

In this chapter, the experimental results obtained are presented. The chapter is divided into two sub-chapters, the first regarding visualization results and the second for force measurement results.

4.1 Flow Visualization

The following studies were performed regarding flow visualization. An enormous quantity of images was acquired for a wide range of possible wing configurations, which were then filtered and systematized to simplify their analysis and presentation.

The presented data was collected in July 2022. The conditions in which the tests were performed are characterized by ambient pressure $P = 926\,\mathrm{hPa}$ and ambient temperature $T = 28\,^{\circ}\mathrm{C}$. These are used to calculate the fluid density using the ideal gas law, $\rho = P/RT$. Dynamic viscosity, μ, was determined using tabulated values. Considering a Reynolds number of $Re \approx 1 \times 10^4$, the resulting equivalent airspeed is $U = 0.79\,\mathrm{m/s}$. The true airspeed is then determined using the formula $V = U \times \sqrt{\frac{1.225}{\rho}}$.

The resulting true airspeed is $V = 0.85\,\mathrm{m/s}$. The resulting data is then orderly presented for the series of performed studies regarding relevant conclusions.

4.1.1 Interference of the gap in the lower surface

The first analysis that was done on the developed wing design consists of the observation of the flow around it without any deflection or angle of attack, identical to a NACA0012 airfoil. With this analysis is possible to understand the influence of the gap created in the lower surface.

To do so, it was required to capture images of the flow around the wing in both its standard configuration (with the gap towards the floor), and with the wing mounted on the support frame inverted (with the gap towards the ceiling). This was performed in order to better visualize the flow around that area due to the light conditions and camera positioning.

In these images is clearly visible the formation of the von Kármán vortex street in the trailing edge of the wing, which is associated with the production of drag. Afterward, the vortices produced in both upper and lower surfaces tend to mix in the wake.

Comparing the images of the wing in its standard position, Figure 4.1, with the inverted one, Figure 4.2, in the region where the $15\ \mathrm{mm}$ opening exists, the flow does not seem to be affected by its existence.

Figure 4.1: Configuration: $\alpha_0 = 0^\circ$ & $\theta = 0^\circ$.

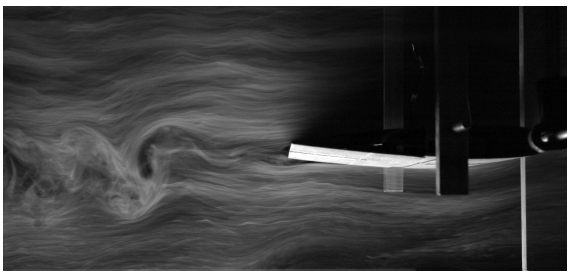

Figure 4.2: Configuration: $\alpha_0 = 0^\circ$ & $\theta = 0^\circ$ - Inverted wing.

4.1.2 Influence of trailing edge deflection for a constant α_0

The second analysis that was performed consists of the observation of the flow around the wing for a constant angle of attack with no flap deflection and multiple trailing edge deflections, so that it is possible to understand the influence of deflection in the wake. The obtained results are shown in Figures 4.3, 4.4, 4.5, and 4.6.

In all the presented images in this subsection, the angle of attack with no flap deflection is $\alpha_0 = 0^\circ$, with the trailing edge deflection being constantly increased for each image.

Figure 4.3: Configuration: $\alpha_0 = 0^\circ$ & $\theta = 0^\circ$.

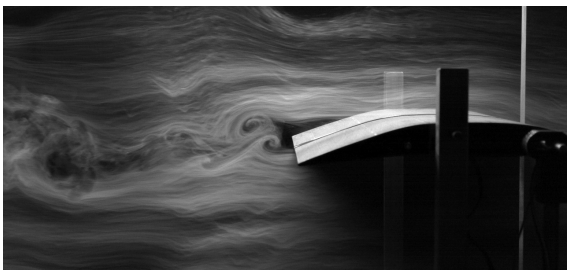

Figure 4.4: Configuration: $\alpha_0 = 0^\circ$ & $\theta = 10^\circ$.

Figure 4.5: Configuration: $\alpha_0 = 0^\circ$ & $\theta = 20^\circ$.

Figure 4.6: Configuration: $\alpha_0 = 0^\circ$ & $\theta = 30^\circ$.

With the increase in trailing edge deflection, it is clearly visible the enlargement of the wake. In that wake, the von Kármán vortex street is also visible in all conditions. In Figures 4.5 and 4.6, the von Kármán vortex street is less perceptible, with the vortices formed in the maximum camber position being caused due to the Kelvin-Helmoltz instability. For lesser

deflections, flow separation happens closer to the trailing edge, even occurring at 50% of the chord for the case of $\theta = 30°$.

One phenomenon that was observed in most configurations is the formation and dissipation of a recirculation bubble in the lower surface of the wing when deflection is imposed on the wing. In Figure 4.7, it is presented the temporal evolution of that bubble, for an $\alpha_0 = 0°$ and $\theta = 30°$ configuration. In order to properly observe it, once again, the wing was placed in the support structure inverted.

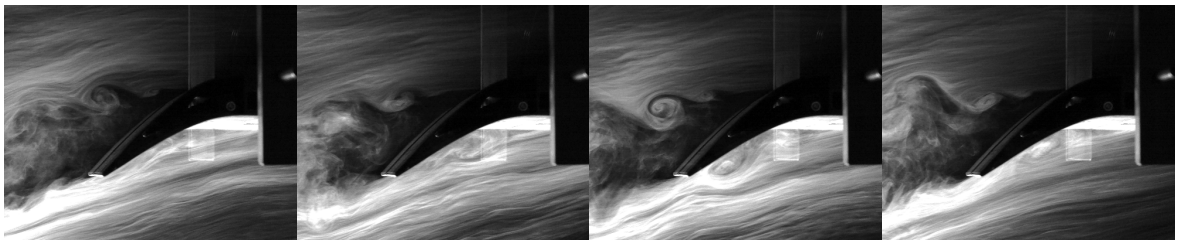

Figure 4.7: Recirculation bubble evolution - Configuration: $\alpha_0 = 0°$ & $\theta = 30°$ - Inverted wing.

From left to right, in the first frame, it is visible a small whirl in the hinge section. That same whirl continuously grows through time until it reaches a considerable dimension. At this moment, the bubble is convected by the passing flow and is pushed through the trailing edge, being then expelled in the edge by the form of a vortex. It is also visible in the last frame that another bubble is being formed near the hinge, indicating that this phenomenon is continuously happening.

It is important to notice that this bubble also forms for lesser deflections, but its dimensions are more reduced than in this case. For the purpose of this thesis, only the presented configuration is shown due to being the most perceptible.

4.1.3 Influence of angle of attack with no flap deflection for a constant θ

The third analysis that was performed consists of the observation of the flow around the wing for a constant trailing edge deflection and various angles of attack with no flap deflection so that it is possible to understand the influence of α_0 in the wing wake. The obtained results are shown in Figures 4.8, 4.10, 4.12, and 4.14, as well as the flow in the lower surface, visible with the inverted wing configuration, in Figures 4.9, 4.11, 4.13, and 4.15.

In all the presented images in this subsection, the trailing edge deflection is $\theta = 20°$, with the angle of attack with no flap deflection being constantly increased for each pair of images.

Analyzing the evolution of the flow, it is perceptible that, on the upper surface, separation only occurs at 50% of the aerodynamic chord. However, on the lower surface, it is visible that negative values of α_0 contribute for separation to occur in the leading edge of the wing, with the formation of vortices quite evident. With the increase in angle of attack, those vortices

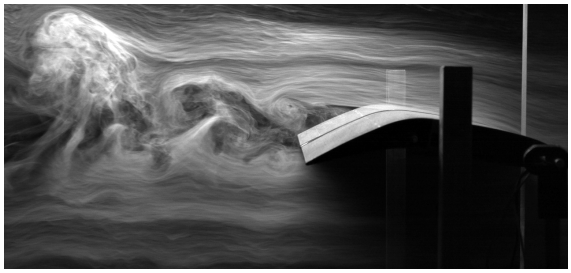

Figure 4.8: Configuration: $\alpha_0 = -10^\circ$ & $\theta = 20^\circ$.

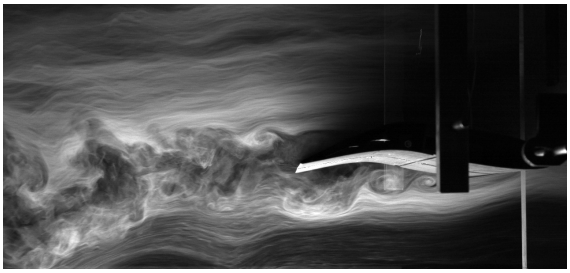

Figure 4.9: Configuration: $\alpha_0 = -10^\circ$ & $\theta = 20^\circ$ - Inverted wing.

Figure 4.10: Configuration: $\alpha_0 = -5^\circ$ & $\theta = 20^\circ$.

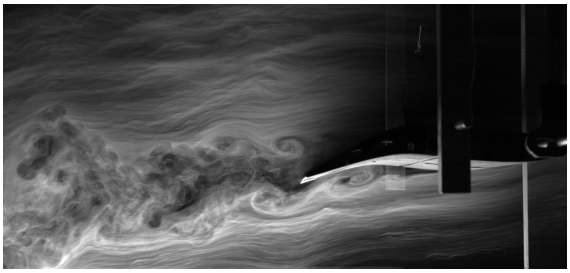

Figure 4.11: Configuration: $\alpha_0 = -5^\circ$ & $\theta = 20^\circ$ - Inverted wing.

Figure 4.12: Configuration: $\alpha_0 = 0^\circ$ & $\theta = 20^\circ$.

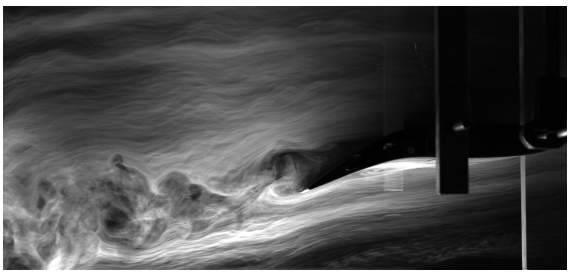

Figure 4.13: Configuration: $\alpha_0 = 0^\circ$ & $\theta = 20^\circ$ - Inverted wing.

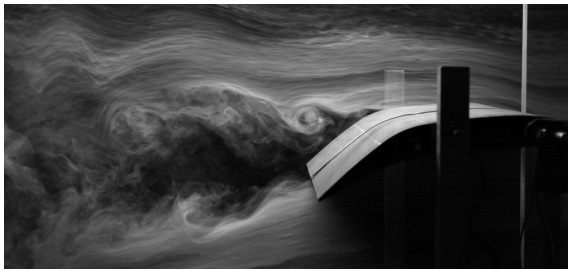

Figure 4.14: Configuration: $\alpha_0 = 5^\circ$ & $\theta = 20^\circ$.

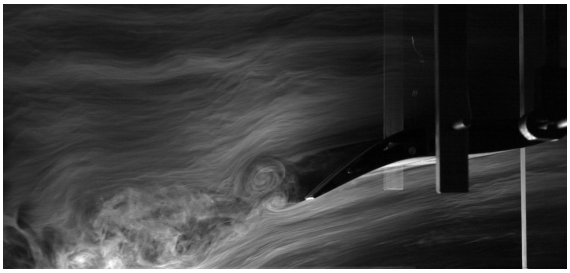

Figure 4.15: Configuration: $\alpha_0 = 5^\circ$ & $\theta = 20^\circ$ - Inverted wing.

reduce in size until no separation is visible, such as in the case of $\alpha_0 = 5°$.

Also, the recirculation bubble described previously in Figure 4.7 is present in the shown cases, being more visible in the configurations with higher camber. Regarding the produced wake, the same appears to not vary its dimension between the featured cases.

4.1.4 Influence of trailing edge deflection and angle of attack combination for a constant α

The fourth analysis that was performed consists of the observation of the flow around the wing for a constant angle of attack and various combinations of $\alpha_0 + \theta$, so that it is possible to understand the influence of each combination in the wing wake for a certain α. The obtained results are shown in Figures 4.16, 4.17, 4.18, and 4.19.

In all the presented images in this subsection, the trailing edge deflection is $\alpha = 15°$, with the angle of attack with no flap deflection being constantly increased and trailing edge deflection correspondingly decreasing for each pair of images in order to obtain a constant angle of attack.

Figure 4.16: Configuration: $\alpha_0 = 0°$ & $\theta = 30°$.

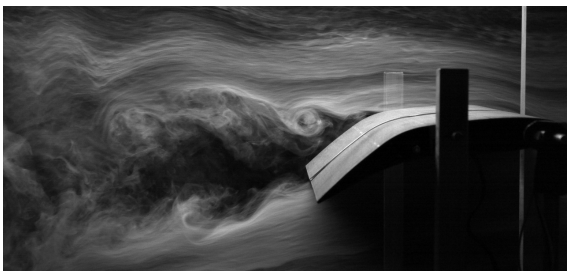

Figure 4.17: Configuration: $\alpha_0 = 5°$ & $\theta = 20°$.

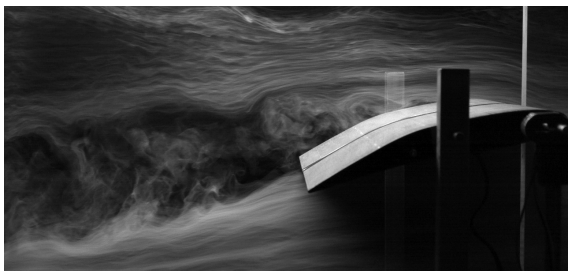

Figure 4.18: Configuration: $\alpha_0 = 10°$ & $\theta = 10°$.

Figure 4.19: Configuration: $\alpha_0 = 15°$ & $\theta = 0°$.

Observing the images, it is clearly visible that the increase in α_0 contributes for moving the flow separation upstream. For instance, in Figure 4.16, separation occurs in the hinge region, while in Figure 4.19, flow separates right in the leading edge. Also, as previously verified, higher deflections reflect in more evident recirculation bubbles.

It is also interesting to comment that the configurations with higher deflection ($\theta = 30°$) or higher angle of attack with no flap deflection ($\alpha_0 = 15°$) are the ones that have massive flow separation with larger wakes.

4.2 Force Measurements

The presented results regard all the obtained data from the experimental studies of force measurements. Values were acquired for a wide range of possible wing configurations, which were then filtered and systematized in order to simplify their analysis and presentation.

The presented data was collected in November 2022. The conditions in which the tests were performed are characterized by ambient pressure $P = 1015\,\mathrm{hPa}$ and ambient temperature $T = 19\,^{\circ}\mathrm{C}$. These are used to calculate fluid density, ρ, and determine dynamic viscosity, μ. Considering a Reynolds number of $Re \approx 2 \times 10^5$, the resulting equivalent airspeed is $U = 14.98\,\mathrm{m/s}$ and the true airspeed is $V = 15.08\,\mathrm{m/s}$

In order to simplify its interpretation, the calculated forces in Equations 3.4, 3.5, and 3.6 were converted into coefficients using the following equations:

$$C_L = \frac{L}{\frac{1}{2}\rho V^2 S}, \tag{4.1}$$

$$C_D = \frac{D}{\frac{1}{2}\rho V^2 S}, \tag{4.2}$$

$$C_M = \frac{M}{\frac{1}{2}\rho V^2 S c}, \tag{4.3}$$

where ρ is the fluid's density, V is the true airspeed of the flow, S is the wing area, and c is the aerodynamic chord.

For the purpose of this dissertation, in every studied wing configuration, the coefficients are obtained assuming the airfoil's non-deformed chord of $c = 0.2\,\mathrm{m}$. When morphed, the airfoil's chord slightly reduces, but this reduction is not significant in the final results. In the most extreme case, that is $\theta = 32^{\circ}$, the chord decreases by $7\,\mathrm{mm}$, which translates into a 3.5% error when comparing the real chord with the assumed one.

The resulting data is then presented in three different manners. Firstly, the study variable is the trailing-edge deflection, θ, as a function of the angle of attack with no flap deflection, α_0. In the second subsection, the study variable is the angle of attack with no flap deflection, α_0, as a function of the trailing-edge deflection, θ. In a third instance, the study variable is the trailing-edge deflection, θ, as a function of the angle of attack, α.

The data is presented in the form of graphs for easier understanding and evaluation.

4.2.1 Aerodynamic Performance as a function of α_0

Figures 4.20, 4.21, and 4.22 show the resulting lift, drag, and moment coefficients, for a range of trailing edge deflections as a function of the angle of attack with no flap deflection. The

moment is always determined at $1/4$ chord of the wing.

Observing the curves in Figure 4.20, it can be noticed that, as expected, with the increase in θ, higher values of C_L can be achieved due to the bigger curvature of the airfoil. With that increase in curvature, wing stall happens at lower values of α_0. Stall can be clearly seen after the wing reaches the maximum value of C_L for each case.

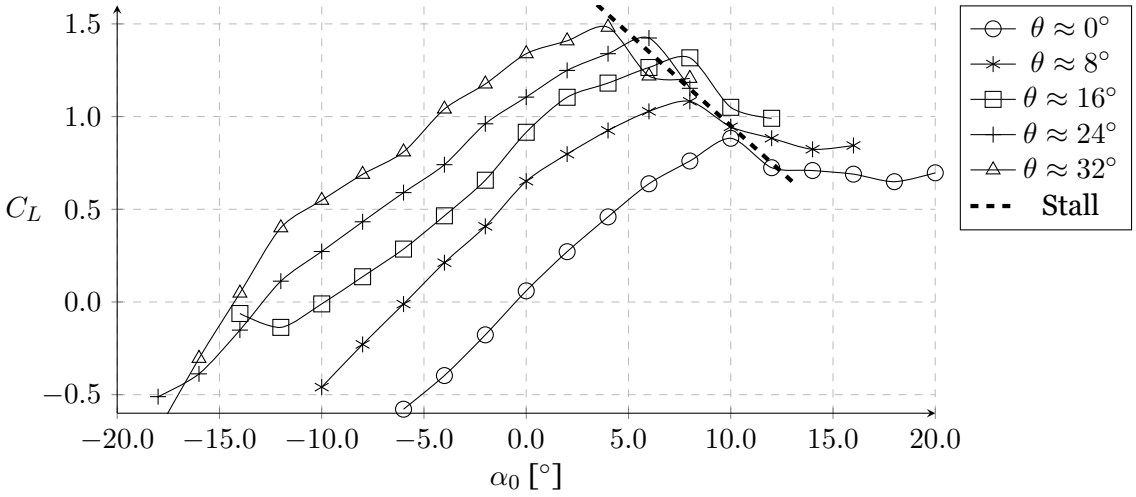

Figure 4.20: Experimental results of the lift coefficient as a function of θ.

Relatively to Figure 4.21, it can be observed that, as expected, bigger values of α_0 tend to reflect in higher values of drag coefficient. The exception happens in the cases of $\theta = 16°, 24°$ and $32°$, for the smallest values of α_0, in which the resultant curvature of the wing results in an increase in C_D.

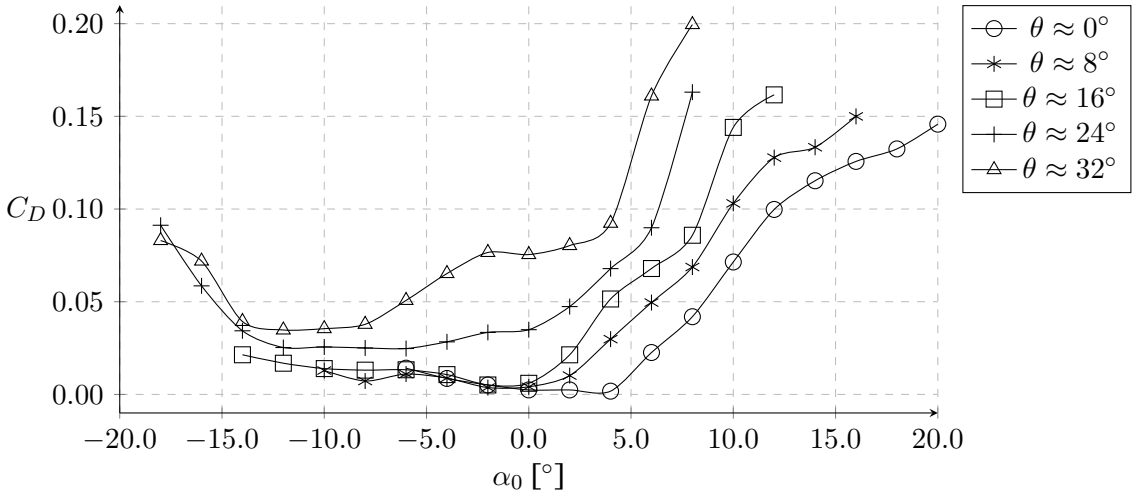

Figure 4.21: Experimental results of the drag coefficient as a function of θ.

Another observation that can be done is that with an increase in trailing edge deflection translates into an increment in drag for a certain angle of attack with no flap deflection.

Also, it is clearly visible that when wing stall happens, an abrupt increase in drag is seen, especially for higher values of trailing edge deflection. These sudden variations appear in

the same corresponding α_0 in which stall is visible in Figure 4.20, for each value of θ.

Analyzing Figure 4.22, it can be seen that, with the increase in trailing edge deflection, there is a clear tendency for the increase of the absolute value of C_M. Also, in almost every wing configuration, the moment coefficient value is negative, showing a nose-down behavior.

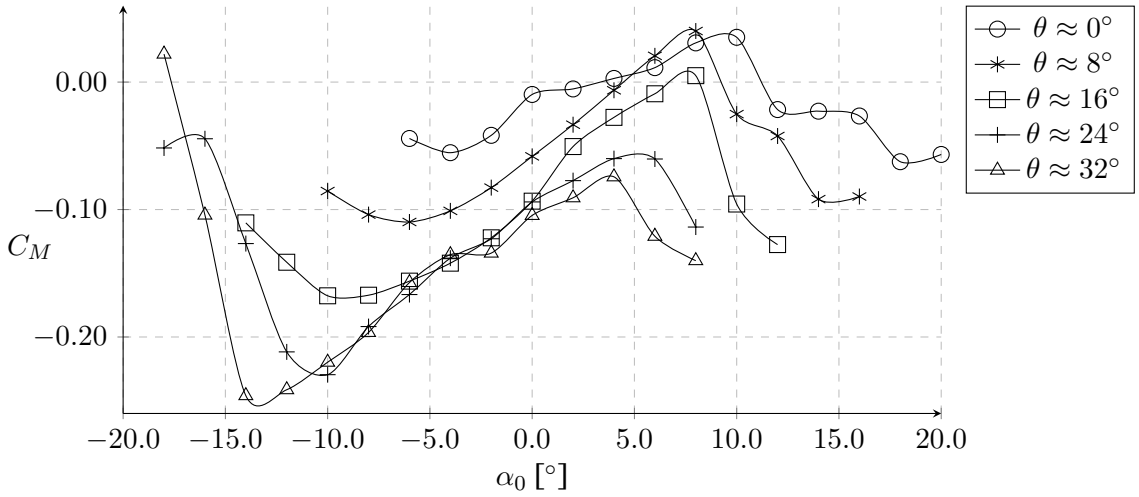

Figure 4.22: Experimental results of the moment coefficient as a function of θ.

Another conclusion that can be withdrawn from this graph is that in the negative part of the α_0 axis, there is a tendency for more abrupt variations in the values of the moment coefficient, clearly visible in the curves of $\theta = 24°$ and $32°$ when $\alpha_0 < -10°$. This is due to the high curvature induced in the wing in this configuration, both in leading-edge inclination and trailing-edge deflection, which reflects in the drag increase.

Similarly to what was noticed in the analysis of C_D, wing stall is well visible through peaks in the value of C_M, in the same values of α_0 in which was observed in the analysis of C_L. For the smaller values of θ, that peak can make the values of C_M to invert the sign and become positive, imposing a nose-up tendency to the wing. However, stall causes a nose-down moment, reestablishing the values of C_M to the negative part of the vertical axis.

4.2.2 Aerodynamic Performance as a function of θ

Figures 4.23, 4.24, and 4.25 show the resulting lift, drag, and moment coefficients, for a range of angles of attack as a function of the trailing edge deflections. These graphs indirectly evaluate the influence of the curvature on the wings' performance.

Observing the curves in Figure 4.23, the immediate conclusion that can be made is that the increase in trailing edge deflection results in the rise of the lift coefficient in each α_0 curve. The only exceptions are visible in the $\alpha_0 = 6°$ and $8°$, in which there are drops in the C_L values when $\theta = 28°$ and $16°$, respectively, due to wing stall. If values of $\theta > 32°$ were achievable with this design, it might be possible to visualize this phenomenon in the curves of smaller α_0.

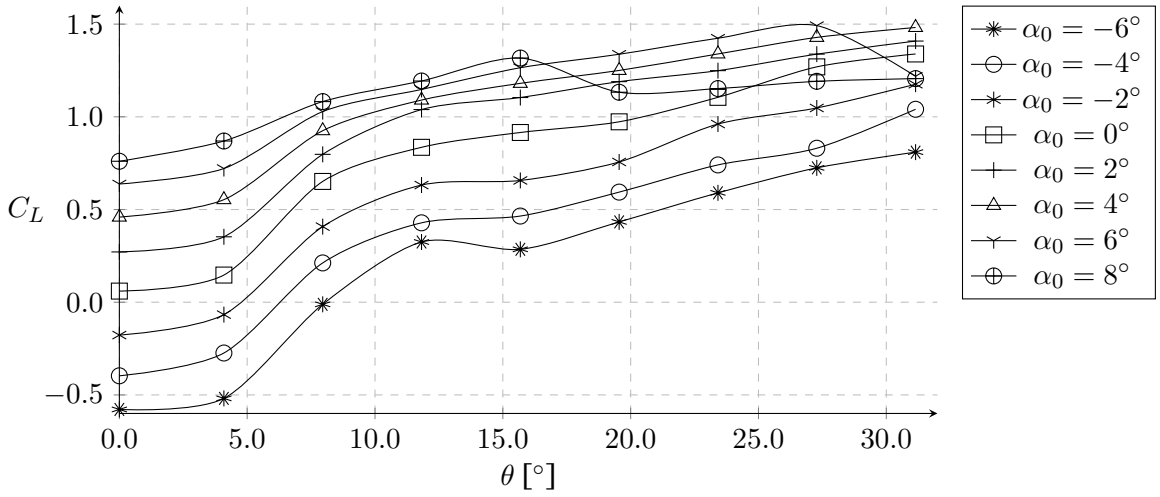

Figure 4.23: Experimental results of the lift coefficient as a function of α_0.

It is also visible that, for smaller values of the angle of attack, there is a sudden increase in the value of C_L when $5° < \theta < 10°$. The introduction of significant camber in the airfoil provides a boost in lift in that region, having a bigger influence for smaller values of α_0.

Another conclusion that is obtained from the graph is that the increase in α_0 generally results in greater values of C_L, as expected. The only exception happens after wing stall occurs.

Since one of the benefits of morphing is the production of less drag for the same quantity of generated lift, that fact can be observed in Figure 4.24. It is possible to see that greater trailing edge deflection manifests in a minimal rise of the values of C_D, with the exception being after wing stall. In these cases, the increase in the drag coefficient is quite accentuated, visible in the curves of $\alpha_0 = 6°$ and $8°$.

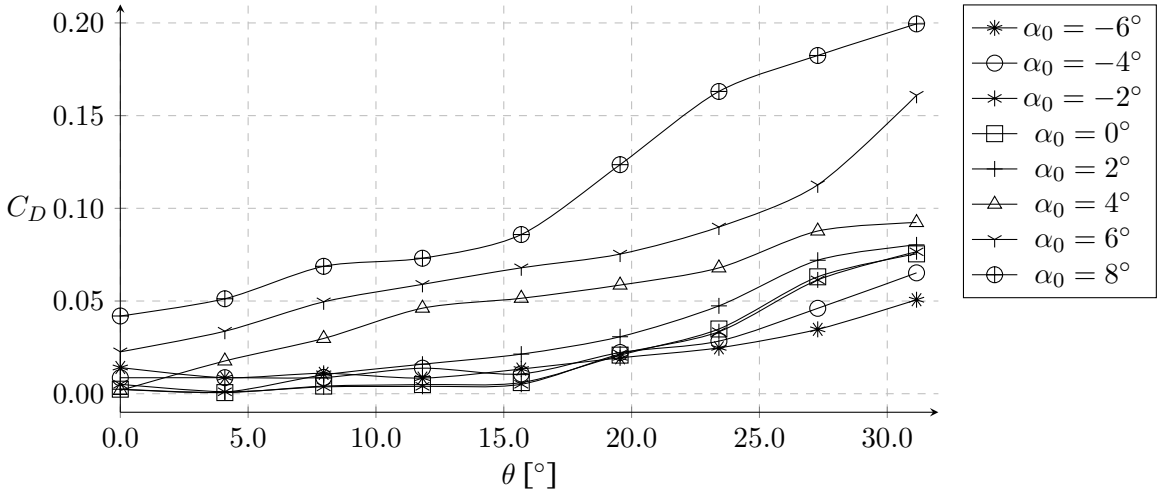

Figure 4.24: Experimental results of the drag coefficient as a function of α_0.

Furthermore, negative and small positive values of α_0 present drag coefficients virtually equal for trailing edge deflection lesser than $\theta = 20°$. This is due to the resultant α being small, and there is not much separation in these configurations.

However, in general, the increase in angle of attack with no flap deflection reflects an increment in drag for a certain trailing edge deflection.

Similarly to what was seen in the drag coefficient graph, Figure 4.25 shows that, in general, the increment in deflection translates into a smooth decrease in the moment coefficient, meaning that the nose-down tendency increases. As seen previously, when stall happens, a sudden nose-down moment appears.

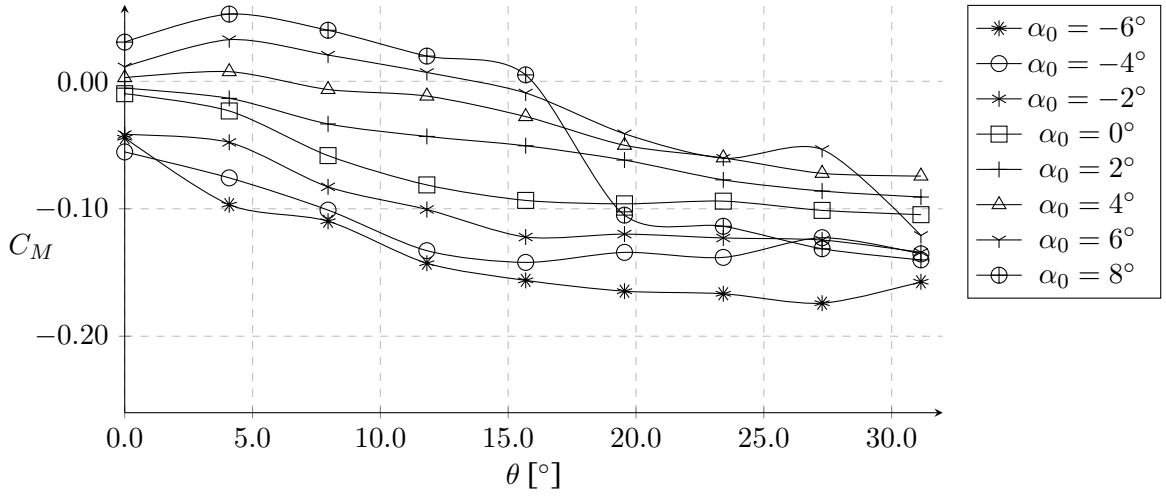

Figure 4.25: Experimental results of the moment coefficient as a function of α_0.

As α_0 increased, for a certain value of θ, the consequent value of C_M also rises, resulting in the curves of higher angles of attack being in the positive region of the vertical axis. This means that the momentum on the wing tends to impose a nose-up tendency that eventually starts decreasing when curvature is incremented, starting to lower the value of the moment coefficient and eventually directing the leading edge of the wing downwards.

4.2.3 Aerodynamic Performance as a function of α

Figures 4.27, 4.28, and 4.29 show the resulting lift, drag, and moment coefficient graphs for a small range of angles of attack as a function of the trailing edge deflections. It is important to remember that $\alpha = \alpha_0 + \theta$. The main goal of this third study is to directly compare the coefficients for the same resulting angle of attack α. The studied configurations, all with the equivalent $\alpha = 10°$, are represented in Figure 4.26.

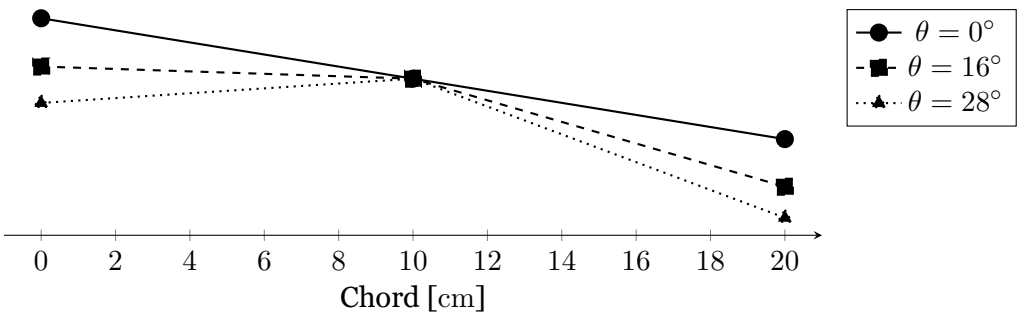

Figure 4.26: Representation of the studied combinations for $\alpha = 10°$.

The first conclusion that can be obtained from Figure 4.27 is that for small angles of attack, independently of the wing's curvature, the quantity of produced lift is similar.

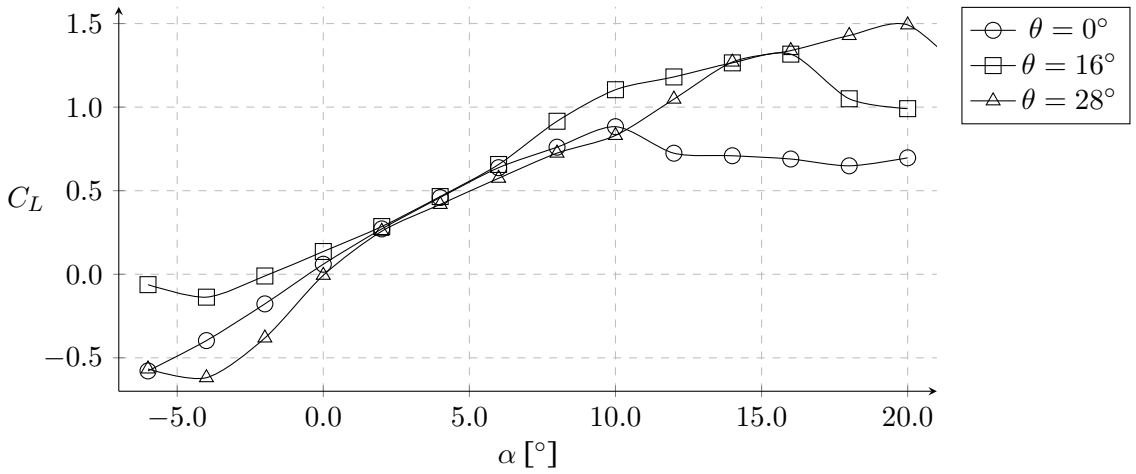

Figure 4.27: Experimental results of the lift coefficient as a function of θ.

However, considering these configurations, stall happens sooner for lesser deflections. So it can be concluded that increasing camber enables the airfoil to achieve higher values of C_L without stall taking effect.

Analyzing Figure 4.28, it can be perceived that the minimum value of drag benefits from the increase in curvature with the evolution of the angle of attack. For instance, when $-5° < \alpha < 5°$, minimum drag is achieved with no trailing edge deflection. As we move forward in the horizontal axis, the drag increases abruptly with the latter configuration but continues at lower values for $\theta = 16°$. It is important to remember that, according to Equation 3.2, until $\alpha = 8°$, the leading edge of this configuration is pointing downwards. The curvature resultant from this combination of α_0 and θ proves to have better performance than the case of no deflection, equivalent to a NACA 0012 airfoil, due to the values of C_L previously presented being identical. A similar occurrence appears when $\alpha = 14°$, but this time for $\theta = 28°$, in which the value of drag is lower for the bigger deflection.

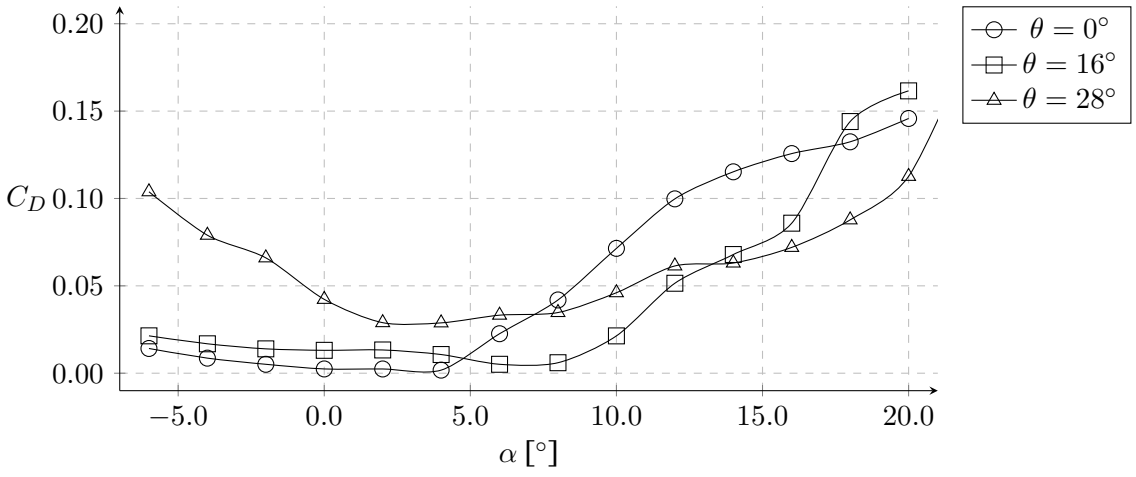

Figure 4.28: Experimental results of the drag coefficient as a function of θ.

With this fact, it is proved that, for a certain angle of attack, adequate camber does not maximize the amount of lift generated, but it does reduce the amount of drag. This means that airfoil camber improves aerodynamic efficiency through the reduction of C_D. Of course that this is only comparable before the wing stalls.

Regarding Figure 4.29, as expected, the more curved a wing is, the bigger the absolute value of its momentum. It is important to notice that, according to Equation 3.2, the bigger the deflection, the lesser the angle of attack with no flap deflection to obtain the desired resultant angle of attack.

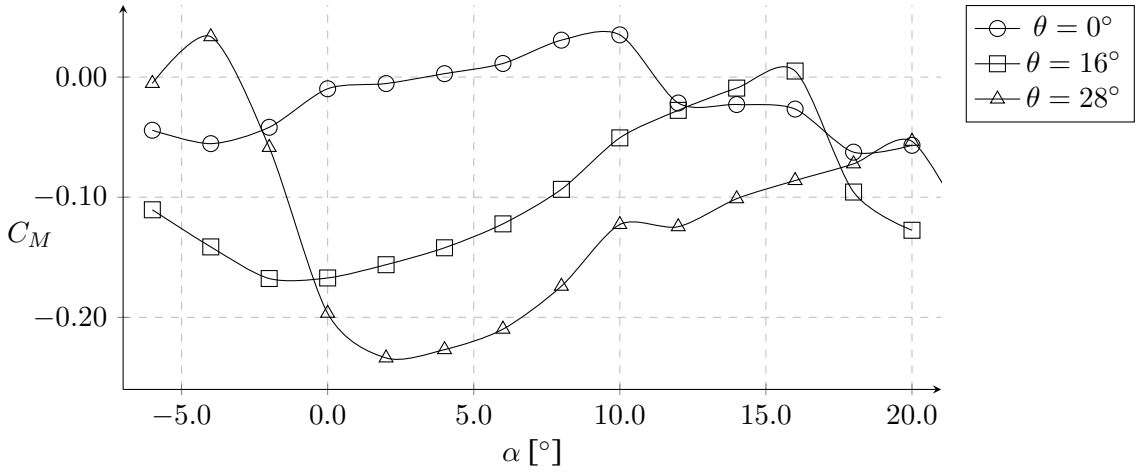

Figure 4.29: Experimental results of the Moment Coefficient as a function of θ.

So, as seen in Figure 4.26, when $\alpha = 10°$, we have $\alpha_0 > 0°$ for $\theta = 0°$ and $16°$, but the leading edge is pointing downwards for $\theta = 28°$. This reflects on the values of C_M being positive, almost positive, and stably negative, respectively. As already stated, positive values of C_M promote a nose-up movement.

On the contrary, for small angles of attack, the moment coefficient is quite significant for the bigger curvatures. This is why the combination of $\alpha_0 + \theta$ should be carefully selected so that no unsuited forces are applied on the wing. But for the values of α mentioned above, the nose-up tendency is not created for the $\alpha_0 + \theta$ combination with the lower value of C_D.

Chapter 5

Conclusions and Future Work

This last chapter is divided into two sub-chapters, the first presenting a conclusion of all the performed work, and the second focusing on future work and propositions to improve the study of morphing.

5.1 Conclusions

Man is constantly trying to improve current technologies in order to make them more productive, economical, powerful, sustainable, and profitable. To do so, bio-inspired concepts have been heavily investigated and applied in modern discoveries due to natural morphology easing the development process due to having been optimized for thousands of years.

Morphing wings have the potential to control the aerodynamic forces of an aircraft in a more efficient way. This dissertation mainly focuses on the process of developing a simple morphing wing. The whole procedure had to be tested and constantly improved to surpass all the challenges that have been encountered due to physical limitations, such as available space inside the wing and material properties, but also the feasibility and effectiveness of the final result.

The electronic part of the system also proved quite challenging due to difficulties coordinating the required energy necessary for powering all components through a single power source without overcharging any component, but also logic-board and servo movement limitations. An important aspect that was taken into account while prototyping was the care to not damage any electronic component to avoid e-waste, extra costs, and time loss.

The resulting wing has a morphing trailing edge able to deflect 32° with a hinge point at 50% of the aerodynamic chord, being controlled with inexpensive and easy-to-use hardware. The components seem sturdy after being submitted to an elevated number of cycles, with minimal signs of wear. However, the actuator and gear are recommended to eventually be replaced in order to ensure the proper behavior of the mechanism.

Regarding visualization, the experimental setup to visualize the aerodynamic performance of the concept had to be developed ahead of testing. The mounting structure was computationally designed and then built, and it enables the wing to be moved across a 3-axis system, as well as rotated in the spanwise direction, increasing the flexibility of the testing process. Combining these capabilities with the resources in the AEROG lab, clear images of the flow

around the wing were obtained, enabling interesting studies of the influence of a certain wing configuration in flow separation. This data allowed for a qualitative evaluation of the developed design.

In terms of force measurement, a wide range of tests was possible to perform at Departamento de Engenharia Mecânica of the University of Coimbra. After some challenges with wind tunnel and strain-gauge balance calibration, a substantial amount of relevant data was possible to obtain. That data contributed to the enrichment of this dissertation considering that it enabled the developed design to be quantitatively evaluated.

This evaluation resulted in interesting conclusions. In general, an increase in the curvature results in higher values for both lift and drag coefficient, with the setback of stall happening for smaller values of α_0. Similarly, for a certain deflection, an increase in the angle of attack with no flap deflection translates into bigger values of C_D.

The increase in the curvature of the wing also contributes to the moment being negative, meaning that no nose-up tendency happens. However, the bigger the curvature, the more abrupt the variations in the value of C_M when varying the value of α. Curvature is an essential parameter that can dictate the nose-up to nose-down tendencies of the airfoil.

For a certain angle of attack, different combinations of $\alpha_0 + \theta$ produce identical amounts of lift, with the difference being in configurations with bigger deflections stalling later. Curvature does not influence the amount of generated lift for a certain α but has a significant impact on drag reduction.

Small combinations of angle of attack with no flap deflection and trailing edge deflection result in a small value of angle of attack, which means that there is not much separation in these configurations.

Stall is clearly visible in the C_L graphs, but it also reflects in the C_D graphs as a sudden increase in drag. In the graphs of C_M, stall is represented as a sudden nose-down moment.

In the latest years, many researchers have been studying morphing surfaces, and designs are constantly being improved mainly to maximize their performance. The latest developments in both materials and structures also contribute to the possibility of large-scale production of components with continuous morphing surfaces, which will undoubtedly show its potential in the near future.

5.2 Future work

The concept of morphing was introduced for the first time in the AEROG research unit via the presented work. It is expected that investigation regarding this innovative, interesting, and exciting topic to be continued in the near future. As already stated, the developed design was conceived to enable aerodynamic studies to be performed as simply and cheaply as possible.

Regarding visualization, it would be interesting to check for a wider range of combinations of angle of attack and trailing edge deflection in order to better associate force measurement patterns with flow phenomena. Dynamic oscillations of the trailing edge can also be considered for future studies, in the pursuit of thrust production. To do so, a precise tuning of the servo motion needs to be performed in order to obtain a sinusoidal oscillation of the trailing edge deflection. The association of this concept with other biomimetic areas can result in a step forward in the quest for bird-like technologies.

Further analysis can include wake measuring using Laser Doppler Velocimetry (LDV) to measure the instantaneous velocity of a flow field after the wing, determining the value of drag for each configuration, and then comparing it with the values obtained with the balance in order to validate them.

Another proposed work could be the update of the designed wing in order to move the position of the hinge closer or further from the leading edge in order to evaluate the effect of the dimension of the morphing surface in the produced wake.

Of course that it would also be interesting to compare the obtained results for the morphing surface with a plain-flapped wing for the same deflection in both wings in order to directly visualize and measure the impact of the continuous surface design when compared to current technologies. In addition, a wider range of Reynolds conditions could be tested in order to check its impact on the developed wing.

The results obtained from this study will be compiled and presented at the 2023 AIAA Aviation Forum & Exposition, as well as in a paper [60].

Bibliography

[1] F. Hao, T. Tang, Y. Gao, Y. Li, S. Yi, and J. Lu, "Continuous morphing trailing-edge wing concept based on multi-stable nanomaterial," *Chinese Journal of Aeronautics*, jun 2020. 1, 2

[2] V. Perricone, C. Santulli, F. Rendina, and C. Langella, "Organismal design and biomimetics: A problem of scale," *Biomimetics*, vol. 6, no. 4, p. 56, sep 2021. 1

[3] J. Hwang, J. Choi, Y. Jeong, J. M. Park, K. H. Lee, and J. W. Hong, "Biomimetics: forecasting the future of science, engineering, and medicine," *International Journal of Nanomedicine*, p. 5701, sep 2015. 1

[4] N. F. Lepora, P. Verschure, and T. J. Prescott, "The state of the art in biomimetics," *Bioinspiration &amp Biomimetics*, vol. 8, no. 1, p. 013001, jan 2013. 1

[5] B. Bhushan, "Biomimetics: lessons from nature–an overview," *Philosophical Transactions of the Royal Society A: Mathematical, Physical and Engineering Sciences*, vol. 367, no. 1893, pp. 1445–1486, apr 2009. 2

[6] D. O. D. Izquierdo and F. D. Marques, "Experimental analysis of passive bio-inspired covert feathers for stall and post-stall performance enhancement," *Meccanica*, vol. 56, no. 11, pp. 2671–2689, jul 2021. 2

[7] I. Dimino, G. Andreutti, F. Moens, F. Fonte, R. Pecora, and A. Concilio, "Integrated design of a morphing winglet for active load control and alleviation of turboprop regional aircraft," *Applied Sciences*, vol. 11, no. 5, p. 2439, mar 2021. 2

[8] A. K. Jha and J. N. Kudva, "Morphing aircraft concepts, classifications, and challenges," in *SPIE Proceedings*, E. H. Anderson, Ed. SPIE, jul 2004. 2

[9] B. W. Jo and T. Majid, "Aerodynamic analysis of camber morphing airfoils in transition via computational fluid dynamics," *Biomimetics*, vol. 7, no. 2, p. 52, apr 2022. 2

[10] S. Barbarino, O. Bilgen, R. M. Ajaj, M. I. Friswell, and D. J. Inman, "A review of morphing aircraft," *Journal of Intelligent Material Systems and Structures*, vol. 22, no. 9, pp. 823–877, jun 2011. 2

[11] Q. Ai, H. K. Jawahar, and M. Azarpeyvand, "Experimental investigation of aerodynamic performance of airfoils fitted with morphing trailing edges," jan 2016. xiii, 2, 8

[12] R. Wu, C. Soutis, S. Zhong, and A. Filippone, "A morphing aerofoil with highly con-

trollable aerodynamic performance," *The Aeronautical Journal*, vol. 121, no. 1235, pp. 54–72, nov 2016. 3

[13] D. Ninian and S. Dakka, "Design, development and testing of shape shifting wing model," *Aerospace*, vol. 4, no. 4, p. 52, nov 2017. 3

[14] K. Dhileep, D. Kumar, S. Ghosh, S. F. Ali, and A. A, "Numerical study of camber morphing in NACA0012 airfoil," in *AIAA AVIATION 2020 FORUM*. American Institute of Aeronautics and Astronautics, jun 2020. xiii, 3, 13

[15] V. de Brederode, *Aerodinâmica Incompressível: Fundamentos*. IST Press, 2014. 3

[16] G. Wang and B. Zhang, "Numerical study on technical and conceptual improvements to a civil aircraft trailing-edge flap using passive/active flow control," *Engineering Applications of Computational Fluid Mechanics*, vol. 15, no. 1, pp. 1362–1391, jan 2021. 3

[17] D. Z. Lima, J. B. Aguiar, and W. G. Ferreira, "Preliminary structural design of a fowler flap high-lifting device," in *SAE Technical Paper Series*. SAE International, mar 2021. 3

[18] D. P. Raymer, *Aircraft Design a Conceptual Approach*. American Institute of Aeronautics Astronautics, 2018. 3

[19] J. Urnes and N. Nguyen, "A mission adaptive variable camber flap control system to optimize high lift and cruise lift to drag ratios of future n3 transport aircraft," in *51st AIAA Aerospace Sciences Meeting including the New Horizons Forum and Aerospace Exposition*. American Institute of Aeronautics and Astronautics, jan 2013. 3

[20] N. T. Nguyen, N. Precup, E. Livne, J. M. Urnes, E. Dickey, C. Nelson, J. Chiew, D. L. Rodriguez, E. Ting, and S. Lebofsky, "Wind tunnel investigation of a flexible wing high-lift configuration with a variable camber continuous trailing edge flap design," in *33rd AIAA Applied Aerodynamics Conference*. American Institute of Aeronautics and Astronautics, jun 2015. 4

[21] S. Gudmundsson, "The anatomy of lift enhancement," in *General Aviation Aircraft Design*. Elsevier, 2014, pp. 401–457. 4

[22] H. Chu, B. Zhang, Y. Chen, Y. Li, and J. Mao, "Investigation of micro vortex generators on controlling flow separation over SCCH high-lift configuration," *Science China Technological Sciences*, vol. 55, no. 7, pp. 1943–1953, may 2012. 4

[23] Y. Tian, T. Wang, P. Liu, and P. Feng, "Aerodynamic/mechanism optimization of a vari-

able camber fowler flap for general aviation aircraft," *Science China Technological Sciences*, vol. 60, no. 8, pp. 1144–1159, dec 2016. 5

[24] N. Nguyen, S. Lebofsky, E. Ting, U. Kaul, D. Chaparro, and J. Urnes, "Development of variable camber continuous trailing edge flap for performance adaptive aeroelastic wing," in *SAE Technical Paper Series*. SAE International, sep 2015. 5

[25] D. Rajendran, "Analysis of morphing airfoil structures and fabrication of the wing using the concept of additive manufacturing," *International Journal of Engineering Research and*, vol. V9, no. 06, jun 2020. 5

[26] D. Hunsaker, J. Reid, and J. Joo, "Geometric definition and ideal aerodynamic performance of parabolic trailing-edge flaps," *International Journal of Astronautics and Aeronautical Engineering*, vol. 4, pp. 1–17, 03 2019. 5

[27] D. F. Hunsaker, J. T. Reid, B. Moorthamers, and J. J. Joo, "Geometry and aerodynamic performance of parabolic trailing-edge flaps," in *2018 AIAA Aerospace Sciences Meeting*. American Institute of Aeronautics and Astronautics, jan 2018. 5

[28] H. K. Jawahar, Q. Ai, and M. Azarpeyvand, "Experimental and numerical investigation of aerodynamic performance for airfoils with morphed trailing edges," *Renewable Energy*, vol. 127, pp. 355–367, nov 2018. 5, 9

[29] Z. Wang, Q. Wu, Y. Lu, P. Bao, Y. Yang, D. Li, X. Sun, and J. Xiang, "Design of a distributedly active morphing wing based on digital metamaterials," *Aerospace*, vol. 9, no. 12, p. 762, nov 2022. 5

[30] N. Tsushima, T. Yokozeki, W. Su, and H. Arizono, "Geometrically nonlinear static aeroelastic analysis of composite morphing wing with corrugated structures," *Aerospace Science and Technology*, vol. 88, pp. 244–257, may 2019. 5

[31] T. Yokozeki, A. Sugiura, and Y. Hirano, "Development and wind tunnel test of variable camber morphing wing," in *22nd AIAA/ASME/AHS Adaptive Structures Conference*. American Institute of Aeronautics and Astronautics, jan 2014. xiii, 5, 6

[32] J. Vale, A. Leite, F. Lau, and A. Suleman, "Aero-structural optimization and performance evaluation of a morphing wing with variable span and camber," *Journal of Intelligent Material Systems and Structures*, vol. 22, no. 10, pp. 1057–1073, jul 2011. xiii, 5, 6

[33] A. D. Gaspari, S. Ricci, and L. Riccobene, "Design, manufacturing and wind tunnel test of a morphing wing based on compliant structures," jan 2016. xiii, 7

[34] H. K. Jawahar, Q. Ai, and M. Azarpeyvand, "Aerodynamic and aeroacoustic performance of airfoils fitted with morphed trailing edges," in *2018 AIAA/CEAS Aeroacoustics Conference*. American Institute of Aeronautics and Astronautics, jun 2018. 9

[35] H. K. Jawahar, M. Azarpeyvand, and C. R. I. da Silva, "Acoustic and flow characteristics of an airfoil fitted with morphed trailing edges," *Experimental Thermal and Fluid Science*, vol. 123, p. 110287, may 2021. 9

[36] D. Communier, R. Botez, and T. Wong, "Experimental validation of a new morphing trailing edge system using price – païdoussis wind tunnel tests," *Chinese Journal of Aeronautics*, vol. 32, no. 6, pp. 1353–1366, jun 2019. xiii, 10

[37] A. H. Ullah, C. Fabijanic, J. Estevadeordal, Z. S. Montgomery, D. F. Hunsaker, and J. J. Joo, "Experimental evaluation of the performance of parabolic flaps," in *AIAA Aviation 2019 Forum*. American Institute of Aeronautics and Astronautics, jun 2019. xiii, 11, 12

[38] V. H. Alulema, E. A. Valencia, D. Pillajo, M. Jacome, J. Lopez, and B. Ayala, "Degree of deformation and power consumption of compliant and rigid-linked mechanisms for variable-camber morphing wing UAVs," in *AIAA Propulsion and Energy 2020 Forum*. American Institute of Aeronautics and Astronautics, aug 2020. 12

[39] T. Majid and B. W. Jo, "Comparative aerodynamic performance analysis of camber morphing and conventional airfoils," *Applied Sciences*, vol. 11, no. 22, p. 10663, nov 2021. 14

[40] Y. Li, W. Ge, J. Zhou, Y. Zhang, D. Zhao, Z. Wang, and D. Dong, "Design and experiment of concentrated flexibility-based variable camber morphing wing," *Chinese Journal of Aeronautics*, vol. 35, no. 5, pp. 455–469, may 2022. xiii, 14, 15

[41] Y. Choi and G. J. Yun, "Variable camber morphing wing mechanism using deployable scissor structure: Design, analysis and manufacturing," *Advances in Aircraft and Spacecraft Science*, vol. 9, no. 2, pp. 103–117, 2022. xiii, 16

[42] A. Rivero, P. Weaver, J. Cooper, and B. Woods, "Progress on the Design of a Composite FishBAC Morphing Device for Spanwise Lift Control," 08 2019. 16

[43] A. Rivero, S. Fournier, P. Weaver, J. Cooper, and B. Woods, "Manufacturing and characterisation of a composite FishBAC morphing wind tunnel model," 10 2018. 16

[44] A. E. Rivero, S. Fournier, R. M. Heeb, and B. K. S. Woods, "Design, manufacture and wind tunnel test of a modular FishBAC wing with novel 3d printed skins," *Applied Sciences*, vol. 12, no. 2, p. 652, jan 2022. xiii, 16, 17

[45] R. Lopes, E. Camacho, F. Neves, A. R. R. Silva, and J. M. M. Barata, "Numerical and Experimental Study of a Plunging Airfoil," in *Proceeding of 4th Thermal and Fluids Engineering Conference*. Begellhouse, 2019. 18

[46] E. Camacho, F. Neves, A. Silva, and J. Barata, "Numerical investigation of frequency and amplitude influence on a plunging NACA0012," *Energies*, vol. 13, no. 8, p. 1861, apr 2020. 18

[47] E. A. Camacho, F. Neves, J. Barata, and A. R. Silva, "Plunging airfoil: Reynolds number and angle of attack effects," in *AIAA AVIATION 2020 FORUM*. American Institute of Aeronautics and Astronautics, jun 2020. 18

[48] D. Rodrigues, E. A. Camacho, F. Neves, J. Barata, and A. R. Silva, "Plunging airfoil motion: Effects of unequal ascending and descending velocities," in *AIAA AVIATION 2020 FORUM*. American Institute of Aeronautics and Astronautics, jun 2020. 18

[49] G. L. Torres, E. A. Camacho, F. D. Marques, and A. R. Silva, "Simulations of a plunging airfoil undergoing unequal ascending and descending velocities at low reynolds numbers," in *AIAA Scitech 2021 Forum*. American Institute of Aeronautics and Astronautics, jan 2021. 18

[50] E. A. Camacho, F. M. Neves, F. D. Marques, J. M. Barata, and A. R. Silva, "Effects of a dynamic leading edge on a plunging airfoil," in *AIAA AVIATION 2021 FORUM*. American Institute of Aeronautics and Astronautics, jul 2021. 18

[51] E. A. R. Camacho, F. M. S. P. Neves, A. R. R. Silva, and J. M. M. Barata, "Plunging airfoil: Reynolds number and angle of attack effects," *Aerospace*, vol. 8, no. 8, p. 216, aug 2021. 18

[52] G. Torres, E. A. Camacho, F. D. Marques, and A. R. Silva, "Theoretical and numerical analysis of oscillating airfoil including viscous effects," in *AIAA SCITECH 2022 Forum*. American Institute of Aeronautics and Astronautics, jan 2022. 18

[53] R. Ferreira, E. A. Camacho, F. P. Neves, J. M. Barata, and A. R. Silva, "Wing design and analysis for micro air vehicle development," in *AIAA SCITECH 2022 Forum*. American Institute of Aeronautics and Astronautics, jan 2022. 18

[54] E. A. Camacho, F. D. Marques, A. R. Silva, and J. M. Barata, "Leading-edge parametric study of the NACA0012-IK30 airfoil," in *AIAA AVIATION 2022 Forum*. American Institute of Aeronautics and Astronautics, jun 2022. 18

[55] S. B. Gonçalves, E. A. Camacho, and A. R. Silva, "Influence of trailing-edge shape on the propulsive performance of a plunging flat plate," in *AIAA AVIATION 2022 Forum*.

American Institute of Aeronautics and Astronautics, jun 2022. 18

[56] J. G. Silva, E. A. Camacho, and A. R. Silva, "Investigation of asymmetric plunging of a NACA0012 airfoil," in *AIAA SCITECH 2023 Forum*. American Institute of Aeronautics and Astronautics, jan 2023. 18

[57] B. Moulton and D. F. Hunsaker, "3d-printed wings with morphing trailing-edge technology," in *AIAA Scitech 2021 Forum*. American Institute of Aeronautics and Astronautics, jan 2021. 24, 25, 29, 38

[58] A. R. Bernardo, "Estudo das características aerodinâmicas de perfis alares," Master's thesis, FCT - Universidade de Coimbra, Sep. 2017. 42, 48

[59] E. N. Jacobs and A. Sherman, "Airfoil section characteristics as affected by variations of the reynolds number," National Advisory Committee for Aeronautics. Langley Aeronautical Lab, techreport 586, 1939. 48

[60] J. Pinho, E. A. Camacho, and A. R. Silva, "Design and testing of a wing with a morphing trailing edge," in *AIAA AVIATION 2023 Forum & Exposition*, 2023. 63

Appendix A

Codes

A.1 For programming the MK10.A

```
#include <Keypad.h>
#include <Servo.h>

// ----------------- KEYPAD CONFIGURATION ---------------------------------------
const byte ROWS = 4;
const byte COLS = 4;
char keys[ROWS][COLS] = {
  {'1','2','3', 'A'},
  {'4','5','6', 'B'},
  {'7','8','9', 'C'},
  {'*','0','#', 'D'}
};

char numbers[10] = {'0','1','2','3','4','5','6', '7', '8','9'};

// ----------------- PINOUT -----------------------------------------------------
byte rowPins[ROWS] = {9, 8, 7, 6}; // Links the pinout of the Keypad to the
    correspondant Arduino pin
byte colPins[COLS] = {5, 4, 3, 2}; // Links the pinout of the Keypad to the
    correspondant Arduino pin

Keypad keypad = Keypad( makeKeymap(keys), rowPins, colPins, ROWS, COLS ); //
    Defines the variable as a Keypad and assign the rows and columns


// ----------------- MOTOR DEFINITION -------------------------------------------
Servo servo; // Defines the variable as a servo motor

void setup() {
  Serial.begin(9600);

// ----------------- MOTOR CONFIGURATION ----------------------------------------
  servo.attach(13); // Links the pin 13 to the servo motor
}

void loop() {

  char key;
```

```
  int pos;

// ----------------- GET KEY FROM KEYPAD ----------------------------------------
  key = keypad.getKey();

  pos = key-48; // Convert ASCII to integer
  // -------------------------------------

// ----------------- EXECUTION --------------------------------------------------
  if (key == '1')
  {
    Serial.print("Servo position:  ");
    Serial.println(pos);

    servo.write(180); // Rotates the servo for the desired position - 180º = No
    deflection
  }
  if (key == '2')
  {
    Serial.print("Servo position:  ");
    Serial.println(pos);

    servo.write(130); // Rotates the servo for the desired position
  }
  if (key == '3')
  {
    Serial.print("Servo position:  ");
    Serial.println(pos);

    servo.write(80); // Rotates the servo for the desired position
  }
  if (key == '4')
  {
    Serial.print("Servo position:  ");
    Serial.println(pos);

    servo.write(30); // Rotates the servo for the desired position - 30º = Full
    deflection
  }
}
```

Servo_Controller_Code_Visualization.ino

A.2 For programming the MK10.B

```
#include <Keypad.h>
#include <Servo.h>

// ----------------- KEYPAD CONFIGURATION --------------------------------------
const byte ROWS = 4;
const byte COLS = 4;
char keys[ROWS][COLS] = {
  {'1','2','3', 'A'},
  {'4','5','6', 'B'},
  {'7','8','9', 'C'},
  {'*','0','#', 'D'}
};

char numbers[10] = {'0','1','2','3','4','5','6', '7', '8','9'};

// ----------------- PINOUT ----------------------------------------------------
byte rowPins[ROWS] = {9, 8, 7, 6}; // Links the pinout of the Keypad to the
    correspondant Arduino pin
byte colPins[COLS] = {5, 4, 3, 2}; // Links the pinout of the Keypad to the
    correspondant Arduino pin

Keypad keypad = Keypad( makeKeymap(keys), rowPins, colPins, ROWS, COLS ); //
    Defines the variable as a Keypad and assign the rows and columns


// ----------------- MOTOR DEFINITION ------------------------------------------
Servo servo; // Defines the variable as a servo motor

void setup() {
  Serial.begin(9600);

// ----------------- MOTOR CONFIGURATION ---------------------------------------
  servo.attach(13); // Links the pin 13 to the servo motor
}

void loop() {

  char key;
  int pos;

// ----------------- GET KEY FROM KEYPAD ---------------------------------------
  key = keypad.getKey();

  pos = key-48; // Convert ASCII to integer

  // -------------------------------------
```

```
45 // ----------------- EXECUTION ---------------------------------------------------

47   if (key >= '0' && key <= '8')
     {
49     Serial.print("Servo position:  ");
       Serial.println(pos);
51
       servo.write(20*pos); // Rotates the servo for the desired position
53   }

55
}
```

Servo_Controller_Code_ForceMeasurement.ino